DESIGN AND PROTOTYPING OF A THREE DEGREES OF FREEDOM ROBOTIC WRIST MECHANISM FOR A ROBOTIC SURGERY SYSTEM

by

TAOMING LIU

Submitted in partial fulfillment of the requirements

for the degree of Master of Science

Thesis Advisor: Dr. M. Cenk Çavuşoğlu

Department of Mechanical and Aerospace Engineering

CASE WESTERN RESERVE UNIVERSITY

January, 2011

CASE WESTERN RESERVE UNIVERSITY

SCHOOL OF GRADUATE STUDIES

We hereby approve the thesis/dissertation of

Taoming Liu

candidate for the Master of Science degree *.

(signed) M. Cenk Cavusoglu
(chair of the committee)

Wyatt Newman

Kiju Lee

(date) August 27, 2010

*We also certify that written approval has been obtained for any proprietary material contained therein.

Contents

List of Tables

List of Figures

Acknowledgements

First of all, I thank my advisor Dr. M. Cenk Çavuşoğlu for letting me involved in this research and appreciate his continuous support and confidence in me. He is a patient and responsible mentor, who not only taught me to solve detailed technical problems, but also gave me enlightening suggestions and optimistic spirit while dealing with failure and disappointments. Furthermore, his encouragement and positive feedback kept me persistently motivated on my research. I am heartily grateful for his help during the past year, which enabled me to complete this thesis step by step.

A special thank goes to my academic advisor, Dr. Kiju Lee. She was willing to listen to me and give me academic guidance. I am also thankful to another member of my committee, Dr. Wyatt Newman. He contributed his valuable time on this committee and offered constructive criticism for this thesis.

I appreciate my lab-mates for their friendly help in my research every day. Their perspectives extended my view of research and their humor enriched our boring research life. Especially, I am grateful to Dr. Özkan Bebek for his insightful ideas and his exhaustive instructions on design and fabrication. Also many thanks to those who gave me the possibility to complete this thesis.

Last but not least, I am indebted to my parents and my younger brother for their excellent care and permanent support throughout my life. I also thank my girlfriend Xinmu for listening my complaints and frustrations, for offering her spiritual support, and for believing in me.

List of Abbreviations

MIS	Minimally Invasive Surgery
MIRS	Minimally Invasive Robotic Surgery
DOF	Degree(s) of freedom
PD	Position-plus-Derivative
PID	Proportional-Integral-Derivative
UCB	University of California, Berkeley
UCSF	University of California, San Francisco
DC	Direct Current
DLR	German Aerospace Center
FDA	Food and Drug Administration
F/T	Force/Torque
EDM	Electron Discharge Machining
SMA	Shape Memory Alloy
PC	Personal Computer
PCB	Printed Circuit Board
I/O	Input/Output

Design and Prototyping of a Three Degrees of Freedom Robotic Wrist Mechanism for a Robotic Surgery System

Abstract

by

TAOMING LIU

In minimally invasive surgery, the dexterity of surgical tools is drastically constrained due to a small entry point on the body. Robot-assisted surgical tool systems can be used to overcome this drawback. In this thesis, a 3 degrees-of-freedom (DOF) robotic arm with 6-axis force feedback for minimally invasive surgery is presented. This prototype contains a 2 DOF spherical wrist, which can pitch $\pm 90^\circ$ and yaw $\pm 35^\circ$, and a gripper with 6 mm diameter and 32 mm length. This end-effector is actuated using DC motors by means of a cable drive mechanism. A 6-axis force/torque sensor allows accurate measurement of end-effector forces.

Chapter 1

Introduction

1.1 Minimally Invasive Surgery

Minimally invasive surgery (MIS), also known as endoscopic surgery, is a surgical technique where procedures are performed with only a small incision or no incision at all. Since the first endoscopic gallbladder removal surgery performed in France by Erich Muhe in 1985, and the first endoscopic cholecystectomy performed in the United States by J.Barry Mckernan and Saye at Marietta, Georgia in 1988, MIS has dramatically affected and developed various surgical subspecialties [3]. Currently, 96% of one million cholecystectomies carried out in U.S. annually are laparoscopic cholecystectomies, which is also the most popular and successfully performed laparoscopic procedure. Endoscopic surgical techniques have since been broadly introduced into gastrointestinal surgery, gynecologic surgery, urologic surgery, subdermal implants, arthroscopic surgery and thoracoscopic surgery.

Compared with open surgery, MIS is less invasive for the same medical purpose. For example, four incisions of 0.5-1.0 cm are necessary in laparoscopic cholecystectomy, while traditional treatment would require at least a 20 cm incision. As a result, MIS benefits the patients in terms of reduction on loss of blood in surgery, trauma to healthy tissue and post-operative pain. It also reduces wound infection risks, and

thus shortens hospital stays and rehabilitation time, which play a substantial role in the cost.

In MIS, a surgeon inserts long and slender instruments through small incisions to reach the intracorporal operation field. A lighted camera, as the eye of the surgeon at the end of one of the instruments, transmits the view of the operation field back to a 2D high-definition monitor. A great many of 5-10 mm diameter surgical tools, such as graspers, scissors, and needle holders, are mounted on the distal end of instruments.

However, MIS suffers from some intrinsic drawbacks. Since only a two dimensional view of the operation field is available, surgeons are unable to be aware of precise distances the surgical tools should move. The configuration of the tools and the viewing equipment result in a degraded hand-eye coordination. This is a challenge for surgeons and requires additional hands-on training besides their basic surgical training. Because of the limited view of the camera, it takes a longer time for a surgeon to master the comprehensive surgical situation. Due to the restriction of the incision point, the dexterity of the instrument is heavily restricted, as 2 DOF is missing inside the patient in contrast to open surgery. Another limitation for surgeons is that they lose the ability of tactile perception, which can facilitate perception of the organ or tissue they are manipulating. The surgeon also deals with the reduced sensation that how much force is exerted on the tips of instruments. As a consequence of the technical complexity of the MIS approach, it takes comparatively longer operating times.

1.2 Minimally Invasive Robotic Surgery

In minimally invasive robotic surgery (MIRS), the surgery is performed by the surgeon using teleoperated robotic tools instead of using manual instruments. In this scheme, robots do not replace the surgeon, but instead provide the surgeon with improved abilities to perform the intricate, precise surgical manipulations.

MIRS aims to overcome the drawbacks of conventional MIS by a teleoperated approach. During MIRS, surgeon could comfortably sit at a console beside the patient and control robotic arms by a joystick-like controller. One robotic arm holds a 3D camera transferring the view of operating field back to monitor, while other arms hold specially designed and miniaturized surgical tools, and precisely imitate the surgeon's hand movements in real world. Staring at a vivid 3D image from the camera in the patient body, the surgeon with a pair of 3D glasses can take a direct view to the operation field as in open surgery.

The main advantage of MIRS is its capability to provide surgeon with additional DOF to control surgical tools at the distal end of instruments and a 3D view of the surgical site as in open surgery. The purpose of MIRS is to recover or even surpass the dexterity and precision of open surgery. In addition, being able to comfortably sit rather than stand, the physical fatigue of the surgeon can be reduced. Besides, surgeon's intrinsic hand tremors in conventional MIS can be filtered out by the control algorithm and hand movements can be scaled down to perform precise manipulations at smaller strokes. In addition, surgical systems can alert the surgeon the magnitude of the thrust force on the distal surgical tool and gripping force by integrated sensors.

However, current MIRS also has its disadvantages in terms of initial acquisition and maintenance costs, lack of haptic and force feedback, as well as long operating time and set-up time. Nevertheless, MIRS is acknowledged as a promising surgical technology. Numerous scientists are willing to contribute to improving the performance and abilities of robotic surgery systems.

1.3 Motivation

In conventional MIS, the surgeon inserts the surgical tool through a 5-15 mm incision point to get into the skin. As the entry point on body acts like a fulcrum point, the surgical tool is constrained to 4 DOF maximally, causing significantly decreased

dexterity when surgeon manipulates surgical tool. In order surgeon to manipulate the surgical tool dexterously as in the open surgery, a novel and dexterous surgical system with at least 6 DOF would be necessary. Main purpose of this thesis is to develop a dexterous surgical instrument with additional 2 DOF.

Another objective of this thesis is to offer surgeon force sensation through the accurate force and torque measurements from the instrument tip. In MIS, due to long instruments with fixed fulcrum points and increased friction, it is hard for the surgeons to get a clear sense of how much force and moment they are exerting. Therefore, we plan to incorporate force/torque sensors in the instrument to collect precise data of interaction forces.

1.4 Thesis Outline

Chapter 2 introduces an overview of the state-of-the-art of robotic surgical systems for MIRS, including prototypes built in research institutes and commercial products. It also presents various motion modes of surgical instruments. Chapter 3 describes the design principle of our prototype and set up performance specifications in terms of previous literature and needs of surgeon performing MIRS. A variety of articulation mechanisms and power transmissions are discussed and the principles of cable drive mechanism we selected are also introduced in this chapter. In Chapter 4, the kinematics of our prototype is presented. The description of mechanical hardware components and electrical hardware of the prototype and control design are described. Chapter 5 presents the test results of the prototype including range of motion, speed of motion, forces and torque measurement, gripping force measurement and gripper cycle-time. Finally, in Chapter 6, the conclusion is given and future work and further improvements are proposed.

1.5 Contributions

In this thesis, a precise, dexterous, and lightweight prototype of 3 DOF robotic wrist mechanism with force and torque feedback is designed, built and tested. Position control of the instrument with a simple PID control algorithm is presented. With the prototype introduced in this thesis, dexterity of the laparoscopic instrument is increased and the force awareness for the surgeon is realized.

Chapter 2

Background

2.1 Current Development of Robotic Surgical Systems for MIRS

The first robot used in a surgical application was Puma 560, which was used to perform neurosurgical biopsies by Kwoh *et al.* in 1985 [4]. Since then, numerous surgical robots developed at a fast-growing pace. Robotic surgical systems for MIRS are one of the promising technologies in surgery today. A variety of prototypes are developed in research institutes and a couple of commercial products obtained FDA authorization. These surgical robots are utilized in hospitals all over the world.

Cavusoglu *et al.* [1] from the Robotics and Intelligent Machines Laboratory of the University of California, Berkeley (UCB) and the department of Surgery of the University of California San Francisco (UCSF) have developed a master-slave robotic telesurgical workstation for laparoscopy. The second generation robotic telesurgical workstation, including slave manipulator and bimanual system and master workstation are shown in Figures 2.1 and 2.2. The slave manipulator includes two stages, the gross positioning stage and millirobot stage. The gross positioning stage, which is responsible for grasping the millirobot and providing 4 DOF for millirobot's positioning,

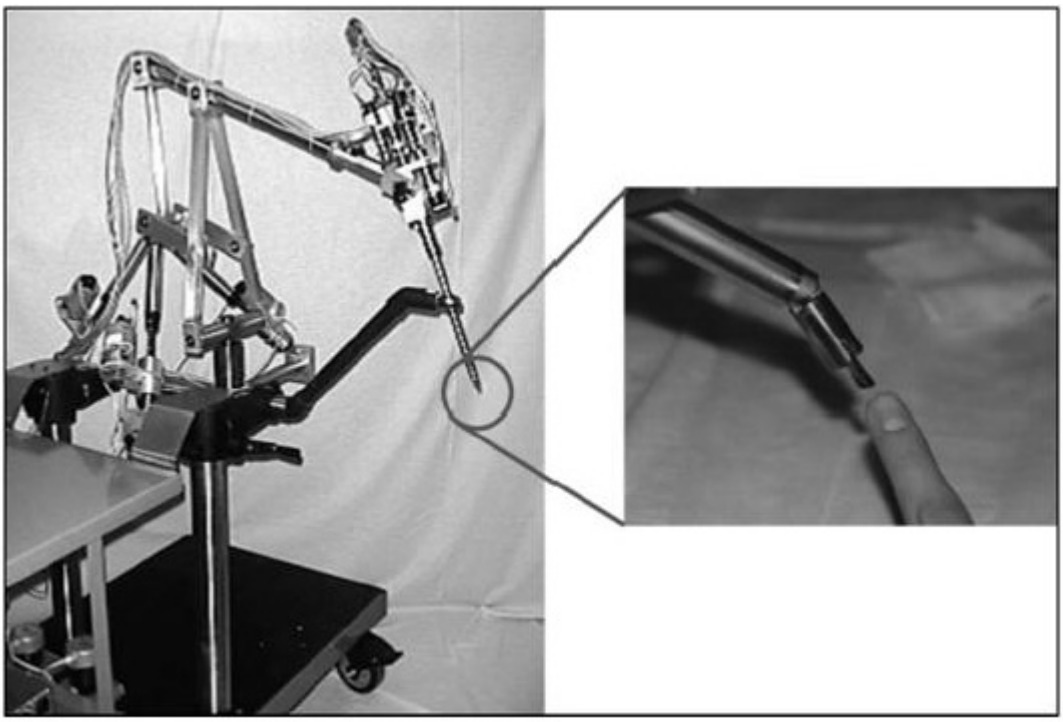

Figure 2.1: A slave manipulator from UCB and UCSF [1].

Figure 2.2: Second generation robotic telesurgical workstation from UCB and UCSF [1].

is located outside the human body. The millirobot with a 2 DOF wrist and a gripper replicates the conventional MIS instrument shown in Figure 2.3. The first stage using parallel manipulator is driven by electrical motors and the second stage is driven by hydraulic actuator. Moreover, the wrist mounted on the millirobot is actuated by tendons jointed by 3 DC motors at the end of tool arm outside the body. The master workstation is designed based on a pair of 6 DOF haptic interfaces, PHANToM (SensAble Technologies, Inc.), each controlling one of the slave manipulators.

Figure 2.3: Summit TR7202 Laparoscopic In Line Needle Holder 5mm x 35cm .

Hagn *et al.* [5] at the Institute of Robotics and Mechatronics of German Aerospace Center (DLR) in Germany have developed the DLR Mirosurge system, a versatile robotic system to be used in endoscopic surgery. This system also adopts a master-slave telemanipulation design. For slave manipulator, three robotic arms are mounted on the operating table, each one holding a DLR MICA instrument at the tip of the arm. Each of these robotic arms resembles a serial kinematics of the human arm with 7 DOF. The DLR MICA instruments working as end effectors are each composed of a functional end, shaft and motor unit, and provides 2 additional DOF to the distal of the instrument. The instruments are responsible for mounting different specially designed and miniature surgical tools.

For the master surgical workstation, they adopt the haptic interfaces as most scientists did and display 3D vision on a monitor reflecting the operation site inside the body. Furthermore, they also mount the reflecting markers on the surgical tool,

which can be tracked by an optical measurement system and map the trajectory of the tip of the surgical tool as the control points.

Several other laboratories also have developed or are developing robotic system for MIRS. Schurr *et al.* [6] at Eberhard Karls University in Germany have developed a master-slave manipulator system named ARTEMIS for laparoscopic surgery, which consists of two robotic arms holding two steerable laparoscopic instruments and a console equipped with two master arms operated by the surgeon controlling the two slave arms. Simaan *et al.* [7] at the Advanced Robotics and Mechanism Applications Research Laboratory of Columbia University are developing a telerobotic system for MIS of the throat and upper airways. They used the da Vinci master interface as their master workstation and designed a dual-arm robotic slave manipulator with a novel flexible snake-like end-effector. They believe that this snake-like end-effector can provide the surgeon with more dexterity inside of the throat. Berkelman *et al.* [8] at the University of Hawaii-Manoa also have developed a compact, less intrusive, tele-operated robotic minimally invasive surgery system. One significant difference is that this surgical module can be placed on the body, which will reduce the requirements of the operating room.

Currently, the da Vinci robotic surgical system (Intuitive Surgical Inc., Sunnyvale,

Figure 2.4: da Vinci Surgical System[2] .

CA) is the most widely used robotic surgery system in market. By 2009, this system has been approved by the FDA for laparoscopic, non-cardiac thoracoscopic, prostatectomy, cardiotomy, cardiac revascularization, urologic surgical, gynecologic surgical, pediatric surgical, and transoral otolaryngology surgical procedures [**?**]. By December 31^{st}, 2009, 1395 da Vinci systems have been installed, 1028 in United States, 9 in Canada, 248 in Europe, 67 in Asia, 11 in Australia, 19 in Middle East, 13 in Latin America [2]. As it can be seen in Figure 2.4, the da Vinci system consists of a master console where the surgeon sits comfortably, and a moveable manipulator, where there are three instrument arms and one camera arm mounted. Additionally, one of the instrument arms is for rapid deployment. With high definition cameras at the end of the camera arm and image processing equipment, the vision system of da Vinci can provide surgeon with the true-to-life 3D images of the operative field. The surgeon's fingers grasp the master controls below the display, with hands and wrists naturally positioned relative to his or her eyes. What's more, the system seamlessly translates the surgeon's hand, wrist and finger movements into precise, real-time movements of surgical instruments inside the patient. For EndoWrist instrument, it is cable driven and designed with 7 DOF that mimic the dexterity of the human hand and wrist.

The Zeus system [2] (Computer Motion Inc., Santa Barbara, CA, merged with Intuitive Surgical Inc., in 2003) has the similar capabilities as the da Vinci system. Zeus robotic surgical system is shown in Figure 2.5. It has been approved by the FDA as well. It is composed of a master console and 3 table-mounted robotic arms. Two robotic arms mimic the surgeon's arms and hold the surgical tool and the third arm is a voice-controlled robotic endoscope named AESOP system. The surgeon also can be seated comfortably in the master console, look at the view of operating field on the monitor and manipulate the instrument handles to control the slave manipulator. The endoscopic instrument mounted on the slave manipulator provides 5 DOF to extend the dexterity inside the patient for the surgeon.

Figure 2.5: Zeus Robotic Surgical System[2].

Chapter 3

System Requirements and Design Principles

3.1 Performance Specifications

The target application of the proposed robotic surgical instrument is minimally invasive cardiothoracic surgery. Specifically, the proposed instrument will be used as a part of a robotic telesurgical system for performing totally endoscopic coronary artery bypass graft surgery at the beating heart. As such, the primary objective of the design is to have an instrument with a 3 DOF wrist, an 8 mm diameter instrument shaft to be able to fit in between the ribs, an actuated needle holder as the end-effector, and an embedded 6 DOF force/torque sensor to measure the end-effector's forces and torques. Suturing is the target surgical task for the system. The schematic representation of suturing is shown in Figure 3.1.

Needles used in MIS are typically curved needles, so that these needles can pinch the tissue easily, rotate circularly inside the tissue and exit. First, the surgeon holds the needle with the needle holder and places the needle on top of the wound, orthogonal to the wound surface, and the tip of the needle points toward either side of the wound. Next, the surgeon thrusts the tip of the needle into the tissue surface

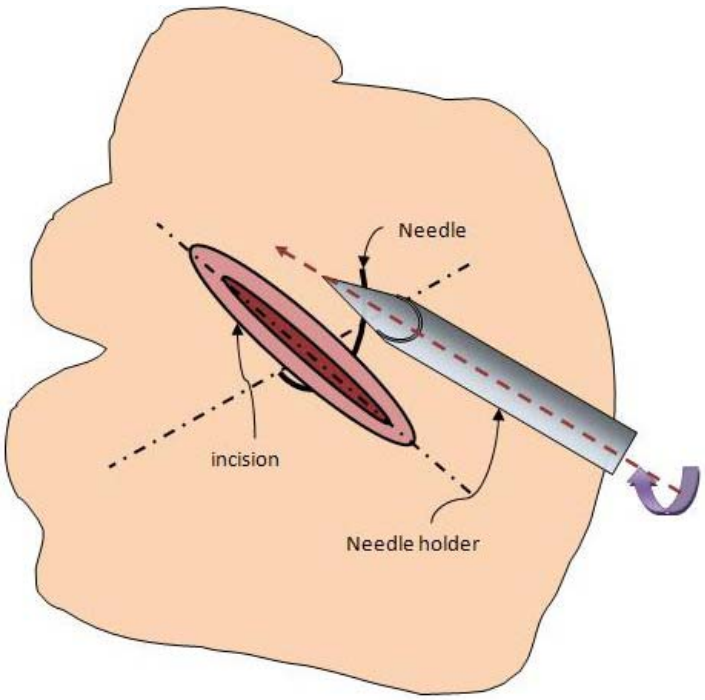

Figure 3.1: Schematic of suturing action .

normally and subsequently, the surgeon rotates the needle circularly along the axis of the arm. After that, the tip of the needle comes out of the tissue on the other side of the wound. Ideally, the path of the needle to complete the action of suture is a perfect circle. However, due to the deformation of the tissue by the thrust of the needle, the entry direction of the needle into the tissue may not be exactly normal. The direction of the wound surface may rotate and the needle should rotate to follow the orientation of the wound surface. During the suture, the large part of the motion needed is the roll motion along the instrument shaft. Additionally, yaw and pitch motions are required for the initial positioning of the needle to get the optimal entry point into the tissue.

Therefore, the instrument should be designed to have at least 3 DOF to orient the end-effector, and an analog actuated gripping action. Performance specifications of the instrument are summarized in Table 3.1. Based on literatures of Cavusoglu et al [9][1], Kode et al [10] and Okamura et al [11], these values are estimated for the

Table 3.1: Performance specifications of prototype

Parameter	**Value**
Shaft diameter	8 mm
Gripping force for holding the needle [10] (Clamping force perpendicular to the surfaces of jaws)	8 N
Force at the tip of needle to perform the thrust [11]	3 N
Torque for orienting the needle	100 Nmm
Range of motion (roll motion) [9]	$\pm 360^o$
Range of motion (pitch motion) [9]	$\pm 45^o$
Range of motion (yaw motion) [9]	$\pm 45^o$
Angle of gripper jaw opening	45^o
Speed of roll motion [1]	540^o/s min
Speed of pitch and yaw motion [1]	360^o/s min

suturing task, force and movement requirements for driving a needle through tissue and tying a knot. The 8 mm diameter shaft is chosen in order to fir the distances between ribs. A roughly measurement of thrust force at the tip of curved needle was tested on a phantom tissue [12], a square sample of silicone rubber (RTV 6186, Momentive) with behavior similar to soft tissues. The rough thrusting force is 2.85 N. Compared with force model for needle insertion into soft tissue developed by Okamura *etal*. [11], the result is similar. So the force at the tip of needle to perform the thrust is set 3 N. Torque, range of motion and speed of motion requirements are estimated from experiments of performing suturing in an open surgical setting [9][1].

3.2 Selection of Articulation Mechanism

The broad objective of this thesis is to design a robotic wrist mechanism for the slave manipulator of MIRS. The significance of the surgical instrument is the dexterity enhancement on the distal end, which requires actuation and power transmission at a millimeter scale mechanism. There are a number of earlier studies in the literature which aimed to restore the dexterity of MIRS tools by introducing additional DOF to the tool tip located inside the body.

Piers *et al.* [13] from Katholieke Universiteit Lweuven in Belgium have developed

a miniature robotic manipulator based on a 3 DOF Stewart platform for a self-propelling endoscope. Driven by the hydraulic pistons or by electromagnetic motors, a Stewart platform can perform combination of angular and linear motions. Reboulet *et al.* [14] have developed a 4 DOF Stewart platform-like parallel manipulator driven by 4 actuators located between a fixed plate and a mobile platform. The mobile platform was jointed on the central pivot by means of a spherical joint. Merlet [15] in France also have developed a micro parallel robot tip with 3 DOF (one translation and two orientations) based on the Stewart platform.

Ikuta *et al.* [16] of Nagoya University have developed a miniaturized prototype of active forceps with 9 DOF for MIS. This manipulator consists of a decoupled ring joint allowing 2 DOF motion, a compensation mechanism for wire elongation, and a detachable gripper mechanism. Simaan *et al.* [7, 17] at Columbia University have developed a newly constructed telerobotic system for MIS of the throat with dual-arm telesurgical slave having 20 joint-space DOF. The distal dexterity unit is composed of two flexible snake-like segments, each of which consists of a base disk, several spacer disks, an end disk, and four flexible super-elastic beams called backbones. The central backbone is called the primary backbone and the three other backbones circumferentially located around the central backbone are called secondary backbones. The distal dexterity unit can rotate in any direction by changing the lengths of two out of the three secondary backbones. Madhani *et al.* [18] have developed a 7 DOF teleoperator slave with a dextrous 4 DOF wrist for MIS. It is a roll-pitch-pitch-yaw wrist driven by cable. Seibold *et al.* [19] have developed an instrument prototype with 6-axis force sensor for MIS. The cable drive actuated distal unit is composed of a 2 DOF cardanic joint, a 6 DOF force/torque sensor and a gripper. Between the cardanic joint and the gripper, a 6 DOF force/torque sensor is mounted on and it can measure the manipulation forces.

Parallel mechanisms can provide the necessary 3 DOF motion, two orientation

motions and one translation motion. Parallel mechanisms typically use four beams moving in a round block, one in the center of the block and three distributed circularly around the disk, and adopt ball-screw mechanisms to transmit the linear motion to actuate the three beams. Due to the complex structure, the parallel wrist would be hard to miniaturize to reach the desired 8 mm diameter. The snake-like designs yield dexterous instruments. Such mechanisms are composed of several same segments to extend the dexterity with multiple DOF, and therefore they need to be long enough to have sufficient workspace and dexterity. As a result, snake-like designs are more suitable to be used in deep and narrow areas, such as throat, ear, and esophagus, and therefore not suitable for thoracoscopic surgery. We prefer adopting a universal joint as our 2 DOF articulated mechanism. Unlike parallel mechanisms, structure of the universal joint without beams and ball-screw mechanisms is simpler and lighter. Unlike snake-like design, the universal joint can be made shorter and more compact. A 2 DOF of universal joint is dexterous enough for thoracoscopic surgery.

3.3 Selection of Power Transmission

Since the proposed instrument will be used to perform MIS, there are strict constraints on the instrument size, which was discussed in Section 3.1. As the planned instrument is going to have an 8 mm instrument shaft, the actuators need to be located outside the body, and the mechanical power for actuating the universal joint needs to be transmitted through the shaft to the wrist, which will located inside the body. The power transmission design from actuator to universal joint plays an important role. There are several transmissions types presented in the literature.

Linkage transmission uses links and gears for power transmission. Rininsland [20] from Karlsruhe Research Center in Germany has built a telemanipulator for cardiac surgery named ARTEMIS with the distal end of the instrument designed as a multi-link structure. Minor *et al.* [21] at Michigan State University have designed

a dexterous manipulator for MIRS with a compact multi-link structure comprised of gears and gear-links to perform bi-directional 180 degree articulation and rotation. Yamashita *et al.* [22] from University of Tokyo in Japan have developed a 2 DOF bending forceps manipulator for intrauterine fetus surgery with linkage drive mechanism.

Yokoi *et al.* [23] developed a 7 DOF manipulator actuated by a tendon drive system. The motor torque from the motor located on the base frame was transmitted to each joint through a tendon-pulley system. Madhani *et al.* [18] adopted the tendon drive mechanism to actuate a roll-pitch-pitch-yaw wrist.

In this thesis, pneumatic transmission was also considered as the power transmission choice for the wrist actuation. It is hard to transmit power from the compressor to the actuator at the wrist through 8 mm shaft. Hydraulic actuation was also considered. However, this actuation scheme has undesirable potential failure possibilities, such as leakage of hydraulic fluid from the hose and the actuators. Hence, hydraulic and pneumatic transmissions are not suitable for our proposed instrument. Due to the instrument size constraint, linkage transmission is not suitable. One reason is that long linkage mechanism inside instrument shaft would increase the weight of the instrument. Another reason is that if the linkage mechanism uses gears, the backlash cannot be avoided, which leads to poor precision and high friction. Cable drive mechanism is more desirable as it leads to almost free backlash and low friction. Absence of links and gears also simplify the universal joint mechanism and reduces the total weight of distal end-effector. Another advantage of the cable drive mechanism is that the actuator could be placed on top of the instrument, where there is less space constraint, instead of near the universal joint. However, if cable is long, it might cause undesirable elastic stretch.

3.4 Principle of Operation of the Cable Drive Mechanism

In the design of the instrument, the cable drive mechanism proposed by Seibold *et al.* [19] has been adopted. This cable drive mechanism uses two motors and a single cable loop to actuate a 2 DOF universal joint wrist, which leads to a lightweight and compact instrument design. In this section, the principle of operation of the drive mechanism is described.

The pitch motion is generated by rotating the two motors in the same direction. The schematic of pitch motion is illustrated in Figure 3.2. In this illustration Motor 1 and 2 rotate counter-clockwise. Then both Pulleys 1 and 2 rotate counter-clockwise. Since Pulleys 1 and 2 are fixed to the lower link of the universal joint, the lower link rotates counter-clockwise. Similarly, Motors 1 and 2 both rotate clockwise, the link rotates clockwise as well.

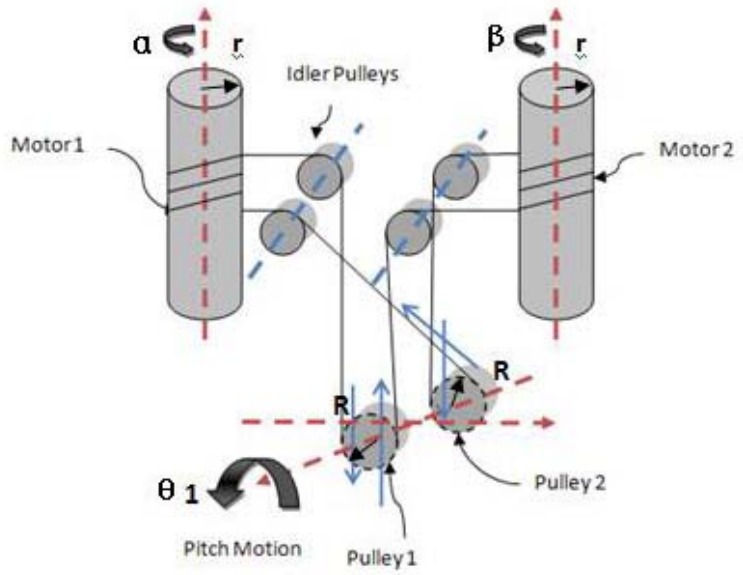

Figure 3.2: Schematic of generating pitch motion .

The relationship between the pitch angle and the rotation angles of the motors 1

and 2 is given as follows,

$$\theta_1 = \frac{1}{2} \cdot (\alpha - \beta) \cdot \frac{r}{R} \tag{3.1}$$

where, θ_1 represents the angle of the wrist's pitch rotation, α represents the angle of the Motor 1 , β represents the angle of the Motor 2, R represents the radius of the pulley in the wrist, and r represents the radius of the adapter of the motor.

The yaw motion is generated by rotating the two motors in opposite directions. The schematic of pitch motion is illustrated in Figure 3.3. Motor 1 rotates counter-clockwise and Motor 2 rotates clockwise. Then pulley 1 gets the extra wire and it is not in tension anymore. In contrast, the pulley 2 is pulled and tautened by the wires on the same direction. As a result, the universal joint rotates toward the direction of tautened pulley.

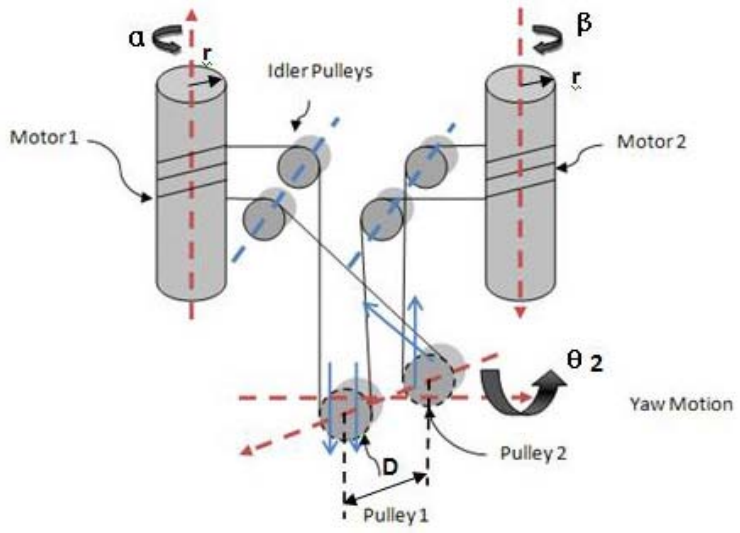

Figure 3.3: Schematic of generating yaw motion .

The relationship between the yaw angle and the rotation angles of the motors 1 and 2 is given as follows,

$$\theta_2 = (\alpha + \beta) \cdot \frac{r}{D} \tag{3.2}$$

where, θ_2 represents the angle of the pitch motion that wrist rotates, α represents the rotating angle of the Motor 1, β represents the rotating angle of the Motor 2,

D represents the distance between the two pulleys in the wrist, and r represents the radius of the adapter of the motor.

Chapter 4

Prototype Design

4.1 Kinematics

In this section, the kinematic analysis of the prototype is described. Forward and inverse kinematics are presented in the following subsections.

4.1.1 Forward Kinematics

The zero configuration and the naming convention is shown in Figure 4.1.

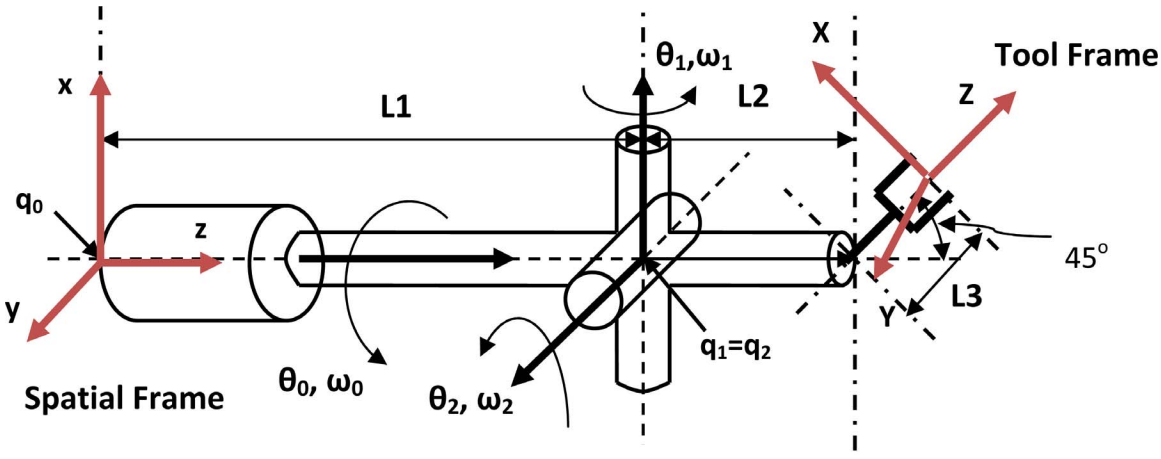

Figure 4.1: Zero configuration of the manipulator.

The kinematic configuration of the manipulator is characterized by the following

vectors and points:

$$\omega_0 = \begin{bmatrix} 0 & 0 & 1 \end{bmatrix}^T \tag{4.1}$$

$$\omega_1 = \begin{bmatrix} 1 & 0 & 0 \end{bmatrix}^T \tag{4.2}$$

$$\omega_2 = \begin{bmatrix} 0 & 1 & 0 \end{bmatrix}^T \tag{4.3}$$

$$q_0 = \begin{bmatrix} 0 & 0 & 0 \end{bmatrix}^T \tag{4.4}$$

$$q_1 = q_2 = \begin{bmatrix} 0 & 0 & L_1 \end{bmatrix}^T \tag{4.5}$$

$$\xi_i = \begin{bmatrix} -\omega_i \times q_i \\ \omega_i \end{bmatrix}, i = 0, 1, 2 \tag{4.6}$$

$$e^{\hat{\omega}_i \theta_i} = I + \hat{\omega}_i \sin\theta_i + \hat{\omega}_i{}^2(1 - \cos\theta_i), i = 0, 1, 2 \tag{4.7}$$

$$e^{\hat{\xi}_i \theta_i} = \begin{bmatrix} e^{\hat{\omega}_i \theta_i} & (I - e^{\hat{\omega}_i \theta_i})(\omega_i \times v_i) + \omega_i \omega_i^T v_i \theta_i \\ 0 & 1 \end{bmatrix}, i = 0, 1, 2 \tag{4.8}$$

where $v_i = -\omega_i \times q_i$.

The transformation between tool and spatial frames at $\theta = 0$ is given by

$$g_{st}(0) = \begin{bmatrix} \frac{\sqrt{2}}{2} & 0 & \frac{\sqrt{2}}{2} & \frac{\sqrt{2}}{2} \cdot (L_3) \\ 0 & 1 & 0 & 0 \\ -\frac{\sqrt{2}}{2} & 0 & \frac{\sqrt{2}}{2} & (L_1 + L_2 + \frac{\sqrt{2}}{2} \cdot (L_3)) \\ 0 & 0 & 0 & 1 \end{bmatrix} \tag{4.9}$$

It can easily be derived that the forward kinematics map of the manipulator is given by

$$g_{st}(\theta) = \begin{bmatrix} R(\theta) & p(\theta) \\ 0 & 1 \end{bmatrix} \tag{4.10}$$

$$R(\theta) = \tag{4.11}$$
$$\begin{bmatrix} \frac{\sqrt{2}}{2}(c_0(c_2 - s_2) - s_0 s_1(s_2 + c_2)) & -s_0 c_1 & \frac{\sqrt{2}}{2}(c_0(c_2 + s_2) - s_0 s_1(s_2 - c_2)) \\ \frac{\sqrt{2}}{2}(s_0(c_2 - s_2) + c_0 s_1(s_2 + c_2)) & c_0 c_1 & \frac{\sqrt{2}}{2}(s_0(c_2 + s_2) - c_0 s_1(s_2 - c_2)) \\ -\frac{\sqrt{2}}{2}c_1(s_2 + c_2) & s_1 & -\frac{\sqrt{2}}{2}c_1(s_2 - c_2) \end{bmatrix}$$

$$p(\theta) = \begin{bmatrix} L_2(c_0 s_2 + s_0 s_1 c_2) + \frac{\sqrt{2}}{2}L_3(c_0(s_2 + c_2) - s_0 s_1(s_2 - c_2)) \\ L_2(s_0 s_2 - c_0 s_1 c_2) + \frac{\sqrt{2}}{2}L_3(s_0(s_2 + c_2) + c_0 s_1(s_2 - c_2)) \\ L_1 + L_2 c_1 c_2 + \frac{\sqrt{2}}{2}L_3 c_1(c_2 - s_2) \end{bmatrix} \tag{4.12}$$

Here, c_0 and s_0 are abbreviations for $\cos\theta_0$ and $\sin\theta_0$, respectively, and similarly for the other terms.

The mapping from the angles of motors to the angles of wrist is derived from equations (3.1) and (3.2) in Chapter 3, as follows:

$$\theta_1 = (\alpha + \beta) \cdot \frac{r}{D} \tag{4.13}$$

$$\theta_2 = \frac{1}{2} \cdot (\alpha - \beta) \cdot \frac{r}{R}. \tag{4.14}$$

Finally, the rotating angle of roll motor equals the angle of roll motion. The equation is given by

$$\theta_0 = \gamma. \tag{4.15}$$

4.1.2 Inverse Kinematics

In order to solve inverse kinematics problem, we need find the set of (θ_0, θ_1, θ_2) triples that drives the end-effector to a desired position, in terms of g_d, the desired configuration of the tool frame shown in Figure 4.1. In Section 4.1.1, we have obtained equations (4.1), (4.2), (4.3), (4.4), (4.5) and (4.9).

The equation we wish to solve is given by

$$g_{st}(\theta) = e^{\hat{\xi_0}\theta_0} e^{\hat{\xi_1}\theta_1} e^{\hat{\xi_2}\theta_2} g_{st}(0) = g_d. \tag{4.16}$$

Postmultiplying this equation by $g_{st}^{-1}(0)$ isolates the exponential maps:

$$e^{\hat{\xi_0}\theta_0} e^{\hat{\xi_1}\theta_1} e^{\hat{\xi_2}\theta_2} = g_d g_{st}^{-1}(0) =: g_1. \tag{4.17}$$

Multiply both sides of (4.17) with point $p_1 \in \mathbb{R}^3$, $p_1 = [0, 1, L_1]^T$ and $\overline{p_1} = [0, 1, L_1, 1]^T$, which is at the axis of ξ_2, but not at the axis of ξ_1 . Since $e^{\hat{\xi_2}\theta_2}\overline{p_1} = \overline{p_1}$, this yields

$$e^{\hat{\xi_0}\theta_0} e^{\hat{\xi_1}\theta_1} e^{\hat{\xi_2}\theta_2} \overline{p_1} = e^{\hat{\xi_0}\theta_0} e^{\hat{\xi_1}\theta_1} \overline{p_1} = g_1 \overline{p_1}. \tag{4.18}$$

Substract from both sides of (4.18) a point $p_0 \in \mathbb{R}^3, p_0 = [0, 0, 0]^T$ and $\overline{p_0} = [0, 0, 0, 1]^T$, which is the origin of the spatial frame. Since $e^{\hat{\xi_0}\theta_0}\overline{p_0} = \overline{p_0}$, this yields

$$e^{\hat{\xi_0}\theta_0}(e^{\hat{\xi_1}\theta_1}\overline{p_1} - \overline{p_0}) = g_1\overline{p_1} - \overline{p_0}. \tag{4.19}$$

Taking the magnitude of both sides of (4.19) gives

$$\|e^{\hat{\xi_1}\theta_1}\overline{p_1} - \overline{p_0})\| = \|g_1\overline{p_1} - \overline{p_0}|. \tag{4.20}$$

Equation (4.20) satisfies Subproblem 3 given in [24], with $p = \overline{p_1}$, $q = \overline{p_0}$, and $\delta = \|g_1\overline{p_1} - \overline{p_0}\|$. The result of θ_1 is obtained by solving the Subproblem 3. The result has either zero, one, or two solutions.

Since θ_1 is known, 4.18 becomes

$$e^{\hat{\xi_0}\theta_0}(e^{\hat{\xi_1}\theta_1}\overline{p_1}) = e^{\hat{\xi_0}\theta_0}\overline{p_2} = g_1\overline{p_1}. \tag{4.21}$$

Applying Subproblem 1 given in [24], with $p = \overline{p_2}$ and $q = g_1\overline{p_1}$, we can obtain the value for θ_0. Equation 4.21 has one solution.

Since we know the values of θ_0 and θ_1, the equation (4.17) becomes

$$e^{\hat{\xi}_2\theta_2} = e^{-\hat{\xi}_1\theta_1}e^{-\hat{\xi}_0\theta_0}g_1 =: g_2. \tag{4.22}$$

Multiply both sides of equation (4.22) to the point $p_0 \in \mathbb{R}^3, \overline{p_0} = [0, 0, 0, 1]^T$, which is not at the axis of ξ_2. This gives

$$e^{\hat{\xi}_2\theta_2}\overline{p_0} = g_2\overline{p_0}. \tag{4.23}$$

Equation 4.23 is in the form of Subproblem 1 [24], with $p = \overline{p_0}$ and $q = g_2\overline{p_0}$, we can obtain the value for θ_2. Equation (4.23) has one solution.

At the end, there are a maximum of two possible solutions.

Based on (4.13) and (4.14), the mapping from wrist angles to motor angles is:

$$\alpha = \theta_1\frac{R}{r} + \theta_2\frac{D}{2r} \tag{4.24}$$

$$\beta = \theta_2\frac{D}{2r} - \theta_1\frac{R}{r} \tag{4.25}$$

where, α represents the angle of Motor 1, β represents the angle of Motor 2, θ_1 represents the angle of yaw motion, and θ_2 represents the angle of pitch motion.

4.2 Description of Prototype's Mechanical Hardware Components

4.2.1 Universal Joint

In the proposed design, the additional 2 DOF on the distal end of the tool is provided by adding a 2 DOF universal joint. In this section, the structure of the universal joint

and the parts included is presented to illustrate the principle and workspace of the universal joint.

4.2.1.1 Structure of Universal Joint

A universal joint, also called Cardan joint, is a widely used component transmitting rotary motion. It consists of two links attached to their respective shafts and connected by means of a spider. The shape of the spider and the link were designed to meet the design requirements, as shown in Figure 4.2.

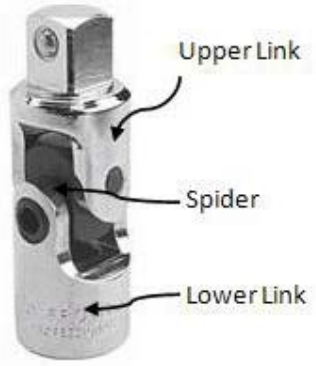

Figure 4.2: Universal Joint (Stanley-Proto J5470A).

The schematic of universal joint is shown in Figure 4.3. It is comprised of two links, upper link and lower link, two pulleys, a shaft and a pin. The links are connected by a cross-like piece, which is formed by a shaft and a pin. The pin goes through the pair of pulleys and the shaft. The pin is press fitted to the pulleys and the lower link, so the pulleys do not rotate relative to the lower link. Additionally, the fit between the pin and shaft is sliding fit, so that the lower link can rotate along the axis of pin. Two sleeve bearings are assembled into the shaft and the upper link, so that the shaft can rotate relative to the upper link.

The shapes of the links are optimized to allow free motion at any direction. They were machined by electron discharge machining (EDM). The outer diameters of the links are 8 mm, satisfying the dimension requirement. There is no clearance between the shaft and the pulleys to prevent unexpected motions.

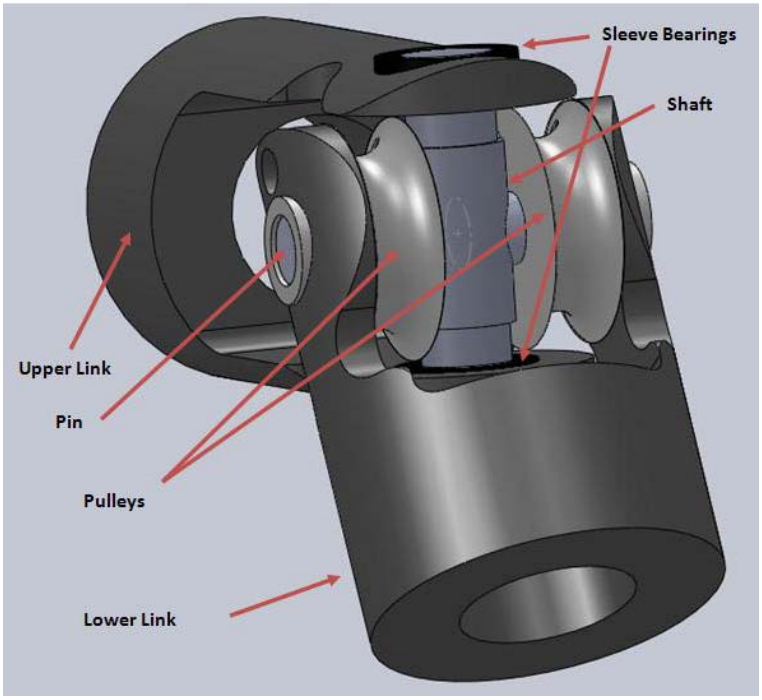

Figure 4.3: Structure of Universal Joint .

4.2.1.2 Workspace of Universal Joint

The workspace of the universal joint is given in Figure 4.4. The range of the pitch motion is from -90^o to 90^o . Due to the intrinsic limitation of universal joint, the range of the yaw motion is from -35^o to 35^o . In Figure 4.4, the distance from the tip of the gripper to the axis of the pin in the wrist is 5.5 mm.

4.2.1.3 Material of Universal Joint

In surgery, the universal joint has to enter human body through the skin barrier. So the materials of universal joint should be taken a full consideration to be bio-compatible with the human internal environment. Moreover, the tendon will exert considerable forces on the pulleys and indirectly on the shaft and the pin. So the materials should be hard enough to suffer the tension from the tendon and also protect themselves from deformation. In addition, it is better to select the common materials in design for simplicity.

In the proposed design, the links, the pulleys and the shaft are made out of type

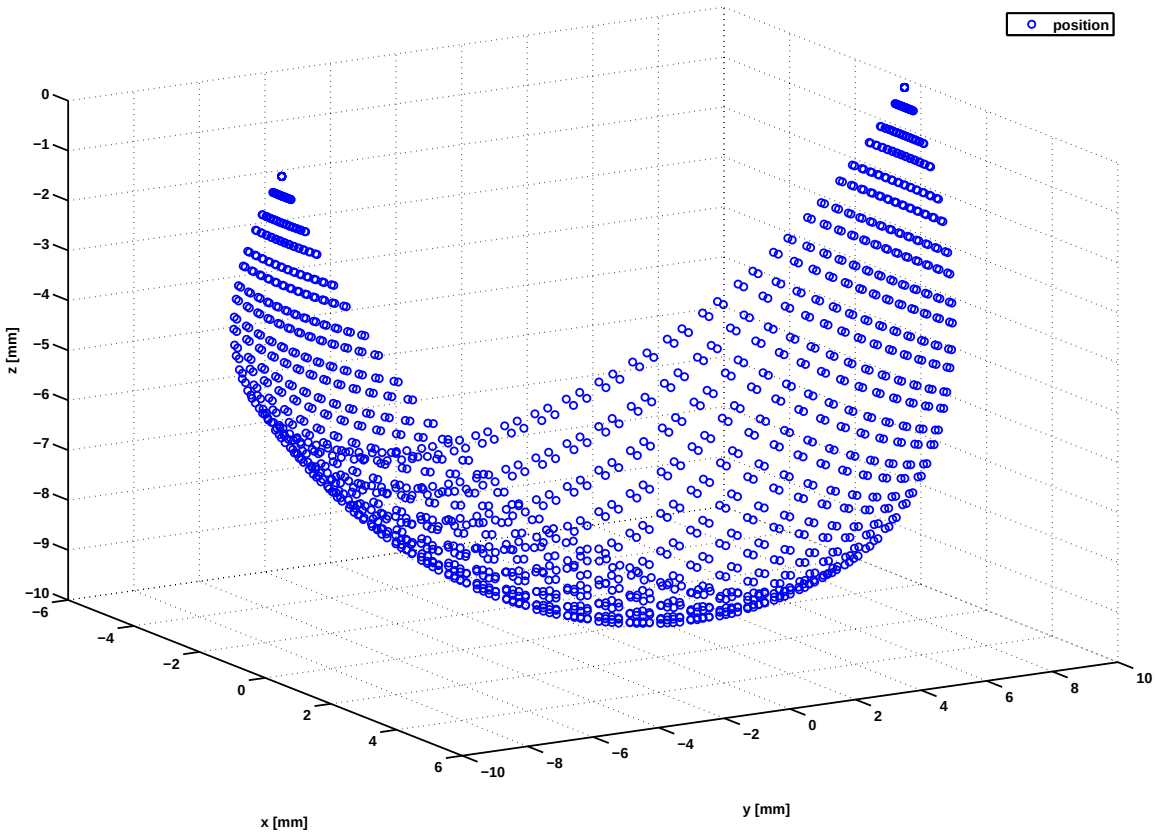

Figure 4.4: Workspace of universal joint

316 stainless steel, which are commonly used in surgical instruments. However, for the sleeve bearings, stainless steel is not a good choice. Because the sleeve bearing is located between the joint shaft and the link, both of which are made out of stainless steels. In order to decrease the friction between them, the coefficient of friction between the material of the sleeve bearings and type 316 stainless steels should be smaller than the one between type 316 stainless steel and type 316 stainless steel. Therefore, PEEK CA30 LSG (QUADRANT, Reading, PA 19612-4235) was a good choice for the sleeve bearings. The coefficient of friction between stainless steel and PEEK is smaller than the one between stainless steel and stainless steel. Although it is a polymer, it has excellent mechanical and chemical resistance properties that are retained to high temperatures. Also, PEEK CA30 LSG is one of the few plastics compatible with ultra-high vacuum applications. More importantly, it is widely used

in surgical instruments, like endoscopic equipments and minimal invasive products.

4.2.1.4 Current Prototype of Universal Joint

Figure 4.5: Prototype of universal joint

The real prototype of universal joint is shown in Figure 4.5. The sleeve bearings in black are made of PEEK CA30 LSG. The upper link is connected with the shaft and the lower link is mounted to the force/torque sensor.

4.2.2 Actuation unit

The actuation unit provides the prototype with the driving forces. Three motors are mounted in the actuation unit, one for roll motion and other two for wrist motions. As it was explained in Chapter 3, the power from the actuation is transmitted to the

joints by tendons.

4.2.2.1 Selections of Motors and Tendon

A. Selection of motors for the wrist motion

This subsection is about selection of motors for the wrist motion, a combination of yaw and pitch motions. The motors are used to drive the gripper to insert needle into the organ tissue during surgery. Okamura *et al.* [11] has developed a force model for needle insertion into soft tissue, which showed that the forces were more than 1.5 N and less than 2.5 N during the needle insertion and removal. The design specification for needle insertion was chosen as 5 N. As shown in Figure 4.6, the distance between the center of the wrist and the line along which the insertion force act, equals (7.874+3+14.5+4+12)×sin(45)=29.25 mm. So the torque that need to be generated at the wrist to achieve the necessary needle insertion force can be calculated as 5 N×29.25 mm=146.258 Nmm.

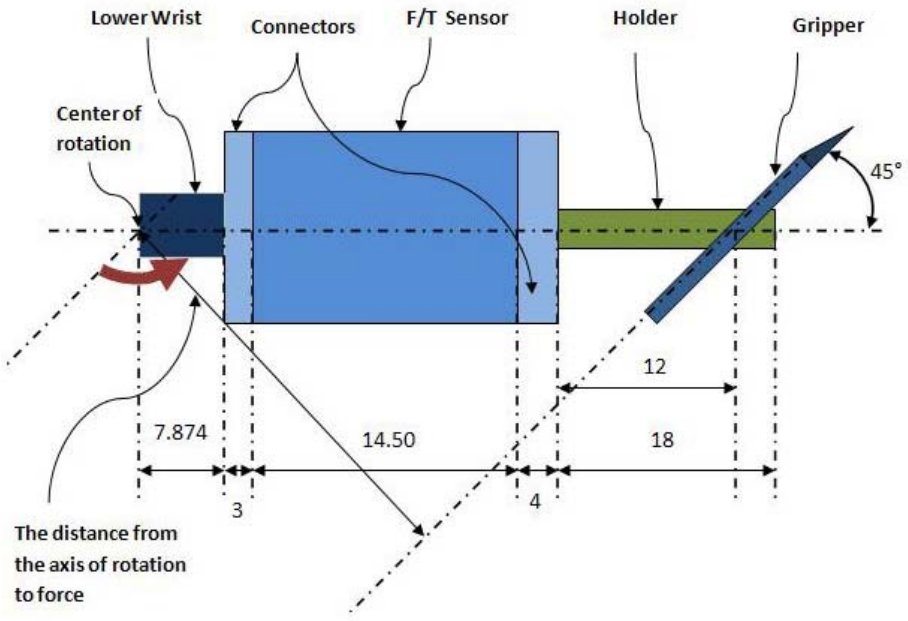

Figure 4.6: Diagram of the calculation of joint force specification from needle insertion force requirements

The torque and force on the wrist was experimentally measured, using an ATI

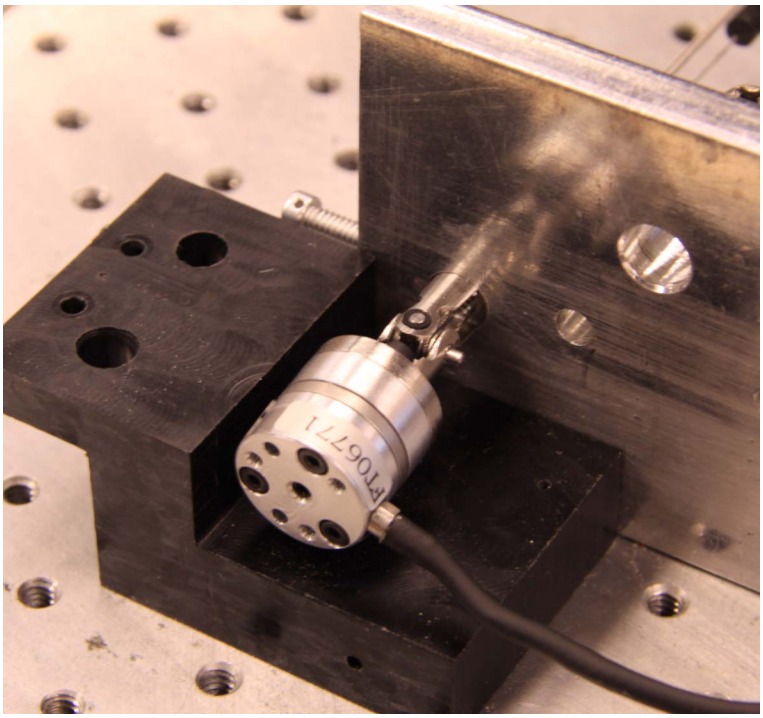

Figure 4.7: Experiment of measuring torque and force

Nano 17 F/T Sensor mounted on the attachment on the wrist. The Figure 4.7 illustrates the experimental setup. As it can be seen from the figure, the gripper is fastened tightly on a metal piece, and a plastic piece is placed next to the sensor to prevent wrist motion, so that stationary forces can be measured.

In this experiment, two Maxon RE 25 precious metal brushes motors were used to actuate the wrist joints. The nominal torque for the motors is 29.1 Nmm at 12.0 volts. Same torque values were applied to both motors which would rotate in opposite directions, resulting yaw motion, and the torques were incrementally increased at 1 Nmm steps starting from 0 to 50 Nmm. Then torque values measured by the sensor were recorded. The collected data and linear fit to the data (R=1.1272) are shown in Figure 4.8. The line equation is $y = 0.4382x - 1.5377$, where x represents the torques from motors and y represents the torques measured at wrist by sensor. We mentioned above that the torque required for the needle insertion was 146.258 Nmm. Using the line equation, $y = 0.4382x - 1.5377$, the result of x is 337.28 Nmm. Because the wrist

design employs 2 motors and the load should be shared by the two motors. So the required torque per motor should be $337.28 \div 2 = 168.64$ Nmm.

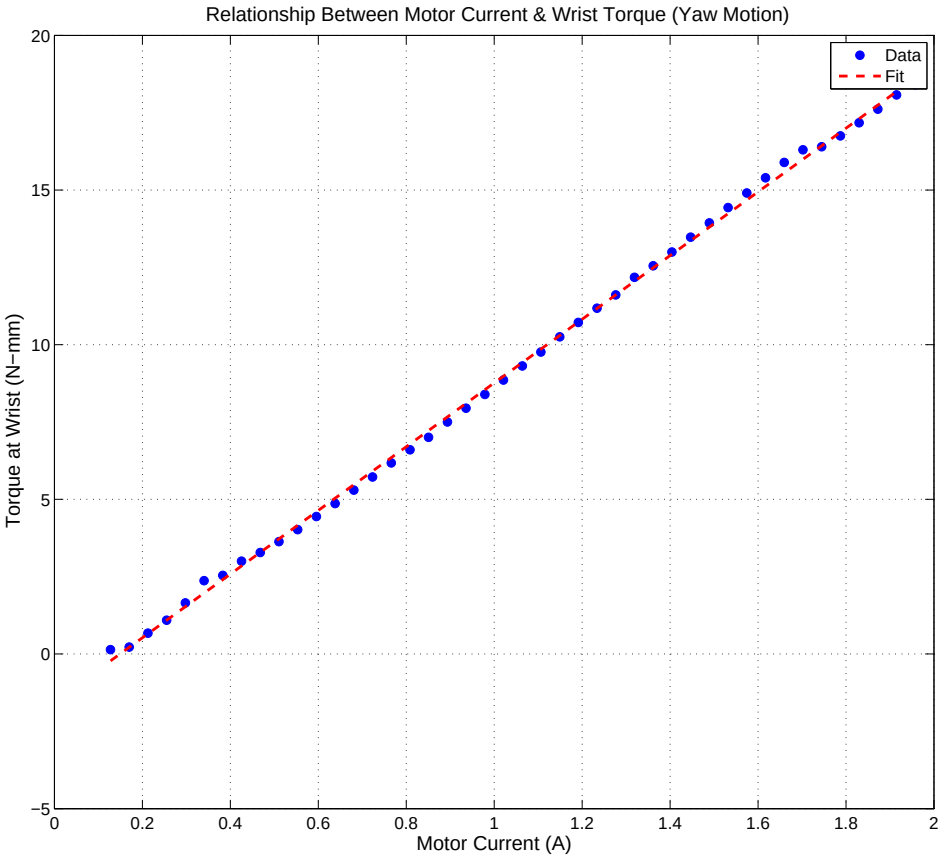

Figure 4.8: Torque Relationship Between Motor and Wrist (Yaw Motion)

The experiment was then repeated by applying motor torques in the same direction, yielding the pitch motion. The collected data and linear fit to the data ,which is $y = 5.6795x - 172.1049$ (R=13.6750) are shown in Figure 4.9. Required needle insertion torque is 146.258 Nmm. From the line equation, we can calculate the result of x given y=146.258 Nmm, which is 63.67258 Nmm. Again, since the torque is shared by two motors, the required torque on each motor is $63.67258 \div 2$=31.83629 Nmm.

Based on the measurements and calculations, a combination of Maxon motor (Part Number 256105) and gearhead (Part Number 218417) was chosen for the wrist

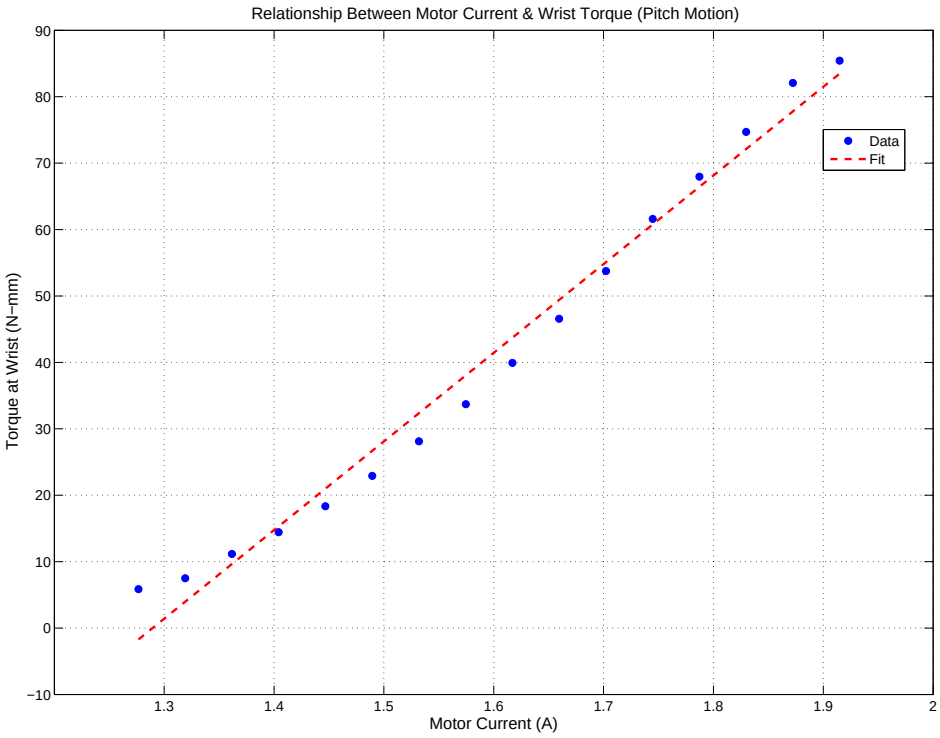

Figure 4.9: Torque Relationship Between Motor and Wrist (Pitch Motion)

actuation. The nominal speed of motor is 6500 rpm and the stall torque is 3.24 Nmm. The reduction ratio of gearhead is 64:1. Therefore, the torque the motor can provide 3.24·64=207.36 Nmm, which is sufficient for this prototype to complete the suturing action. The speed of the motor after the gearhead reduction is 6500 rpm÷64=101 rpm=606 degree/second, which will reach the speed specifications of the yaw and the pitch motions given in Table 3.1.

B. Selection of motor for roll motion

The selection of the motor depends on how much load it is required to rotate the instrument and the speed of rotation required reaching the expected bandwidth. The design schematics of the mechanism are shown in Figures 4.10 and 4.11. The weight of instrument is estimated to be around 500 g according to selected materials and volume of parts. Because centers of mass of many parts, including plates, adapter for

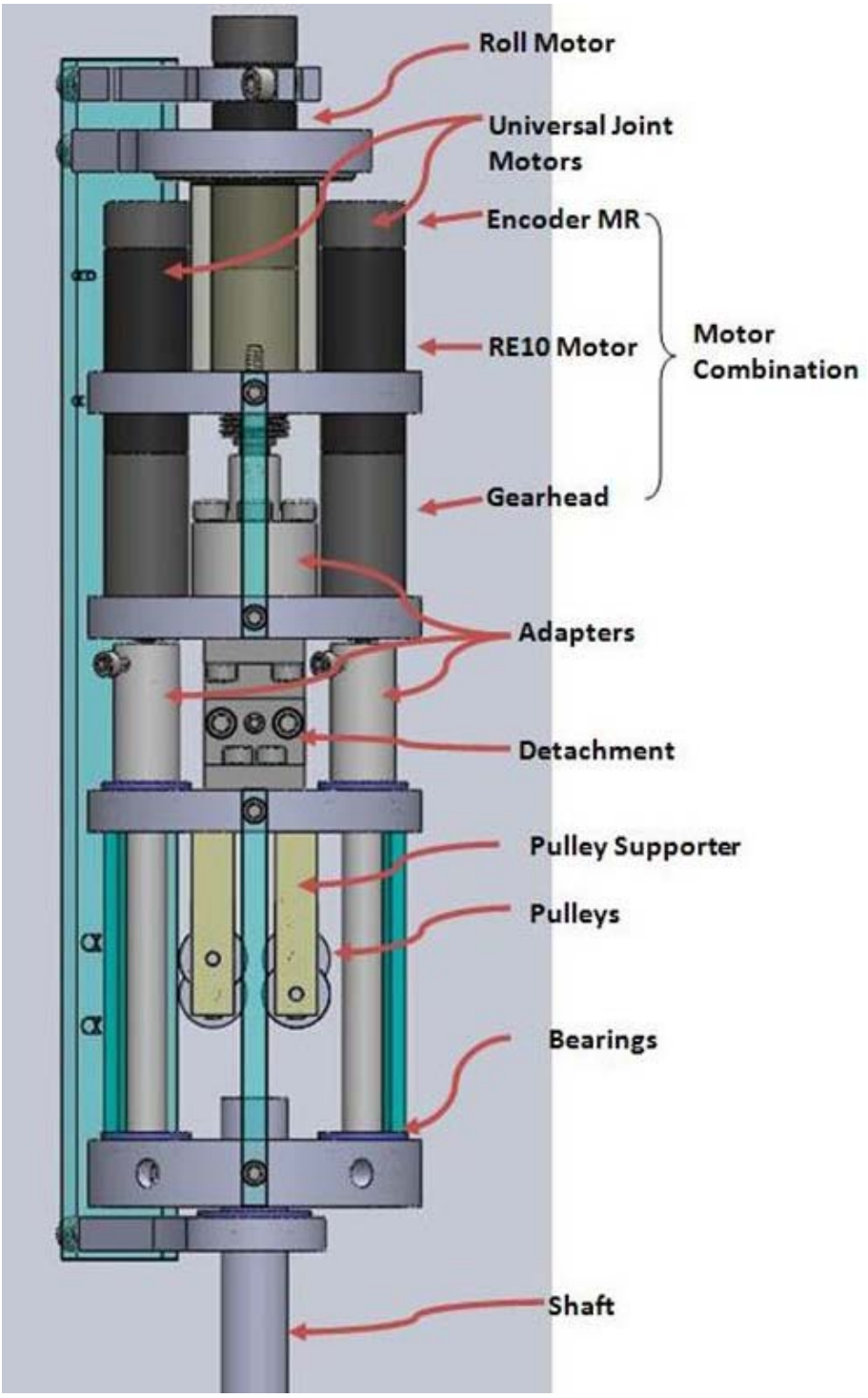

Figure 4.10: Schematic of actuation unit

roll motor, detachment parts, shaft and upper link are almost on the same axis along which the roll motor rotates, the instrument could be estimated as a solid cylinder

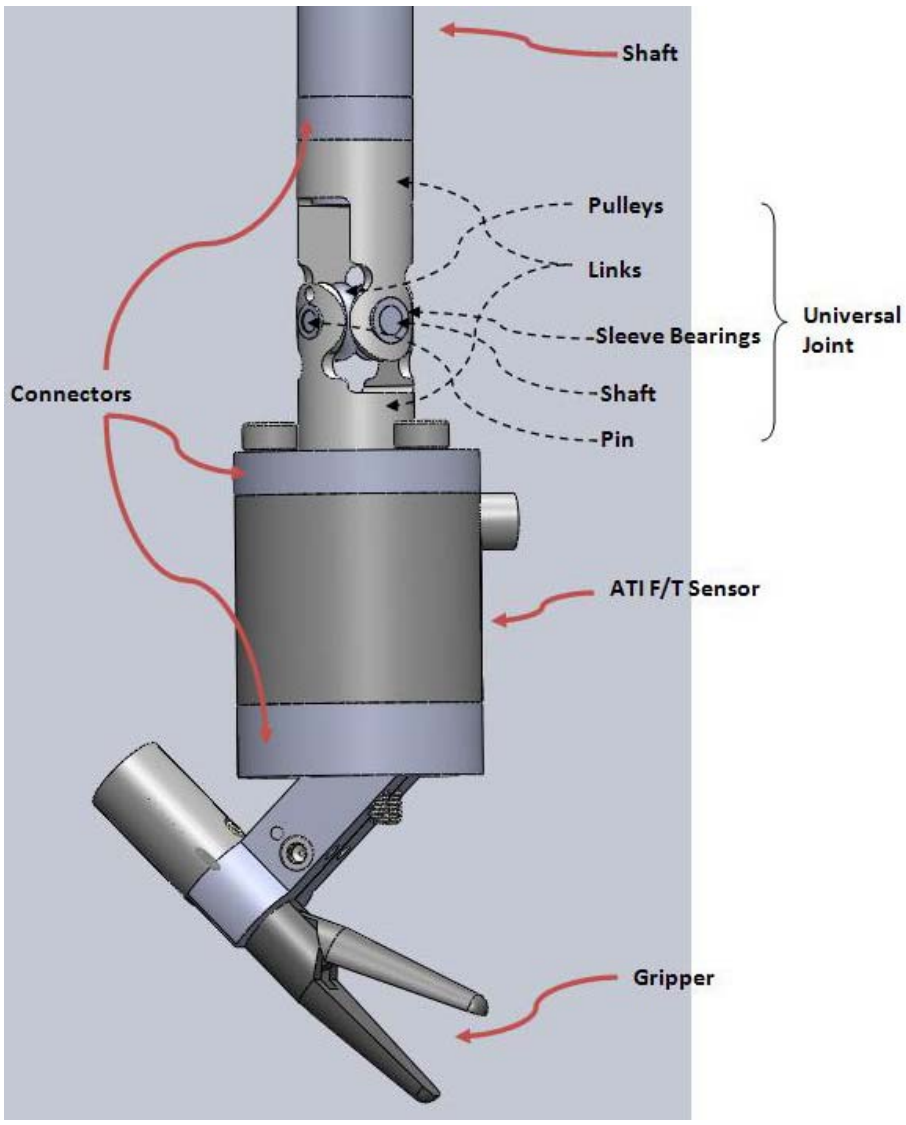

Figure 4.11: Schematic of wrist, sensor and gripper

of radius 20 mm and mass 500 g. The simple model of roll motion is illustrated in Figure 4.12. The equation of moment of inertia is given as follows:

$$J = \frac{1}{8} W D^2 \tag{4.26}$$

where J represents moment of inertia (kg·cm^2), W represents mass (kg), and D represents outer diameter (cm). Based on (4.26), the moment of inertia of instrument along roll motor's rotation axis is $2^2 \cdot 0.5 \div 2$=1 kg· cm^2. The instrument is desired to

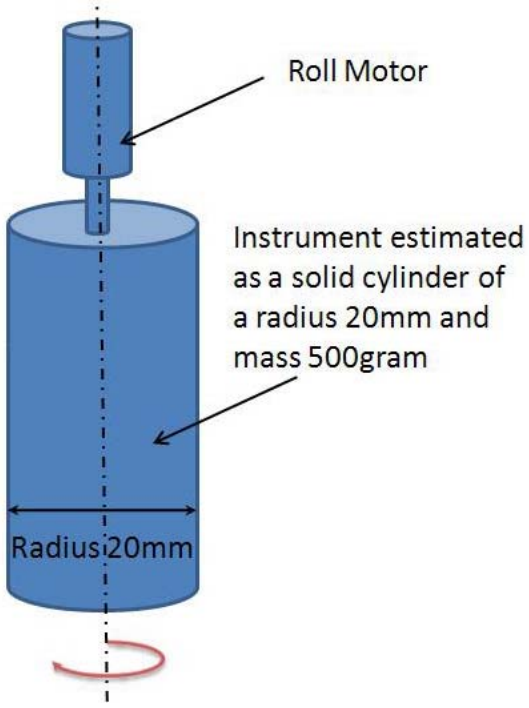

Figure 4.12: Simple model of roll motion in order to calculate moment of inertia and load torque

achieve the speed of roll motion at 540^o/s, then the rotation speed equals $2 \cdot 2 \cdot 60 = 120$ rpm $=720^o$/s. As mentioned in subsubsection 4.2.2.1 A, Maxon motor (Part Number 256105) and gearhead (Part Number 218417) can reach 110 rpm at nominal speed. For convenience, it is desirable to use the same motor selected for the roll motion. As such, it is necessary to verify that this motor satisfies the specifications of the roll motion. The maximal diameter of actuation unit is 40 mm. The equation of load torque of instrument is given as follows:

$$T = J \cdot \dot{\omega} = \frac{J}{9.55 \times 10^4} \cdot \frac{N}{t}(N \cdot mm) \tag{4.27}$$

where, T represents the torque, $\dot{\omega}$ represents the angular acceleration (rad/s^2), N represents rotating speed (min^{-1}), J represents moment of inertia of instrument (kg$\cdot$ cm^2), and t represents the time (s) that motor needs to accelerate the load inertia of J up to a speed N . Compared with the inertia of the load, the motor and the gearhead

inertia, 0.007 kg· cm^2, is ignored. t is assumed to be 0.05 s. So that the load torque is given by T=0.01256 Nm =12.56 Nmm. As presented above, the combination of motor selected for wrist motions can provide 207.36 Nmm torque. It is clear that this motor and gearhead pair is suitable for roll motion as well.

C. Selection of tendon

As discussed in Chapter 3, a tendon drive mechanism was chosen for power transmission. In this subsection, the choice of a qualified cable to meet design requirements is discussed. First of all, the size of the cable is considered to be a critical factor. In this design, due to the miniature nature of the prototype, the size of the cable should also be in the range of 0.015 to 0.025 inches in diameter. The second important factor is the strength of the cable. The motors can produce 80 N forces exerted on the cable. Therefore, the strength of the cable should be at least 25 lbs. Another factor is bend radius of the cable. All cable manufactures specify the minimum bend radius of every cable. Because the cable will be rolled around the pulley, the minimum bend radius of the selected cable should meet the diameters of the pulley.

There are a multitude of different materials used to manufacture cables. Stainless steel is the most common material used for miniature cables. Another metal cable is tungsten wire utilized in light bulb filaments. Tungsten cables are not as widely available when compared to stainless steel cables, and they are not biocompatible. Many synthetic fiber cables are also available, like Spectra fiber, Vectran fiber, and a high-density polyethylene used for fishing line. In this design, type 302 stainless steel cable (Part Number 3458T86, McMASTER-CARR, Aurora, Cleveland. 44202-8087), with 7×3 strand core construction, 0.018 in diameter, 40 lbs breaking strength and 13/32 inches bend radius was chosen.

4.2.2.2 Current Prototype of Actuation Unit

The Figure 4.13 gives the front view of the actuation unit. The roll motor is located on the top and center of actuation unit. Two other motors for wrist motions are

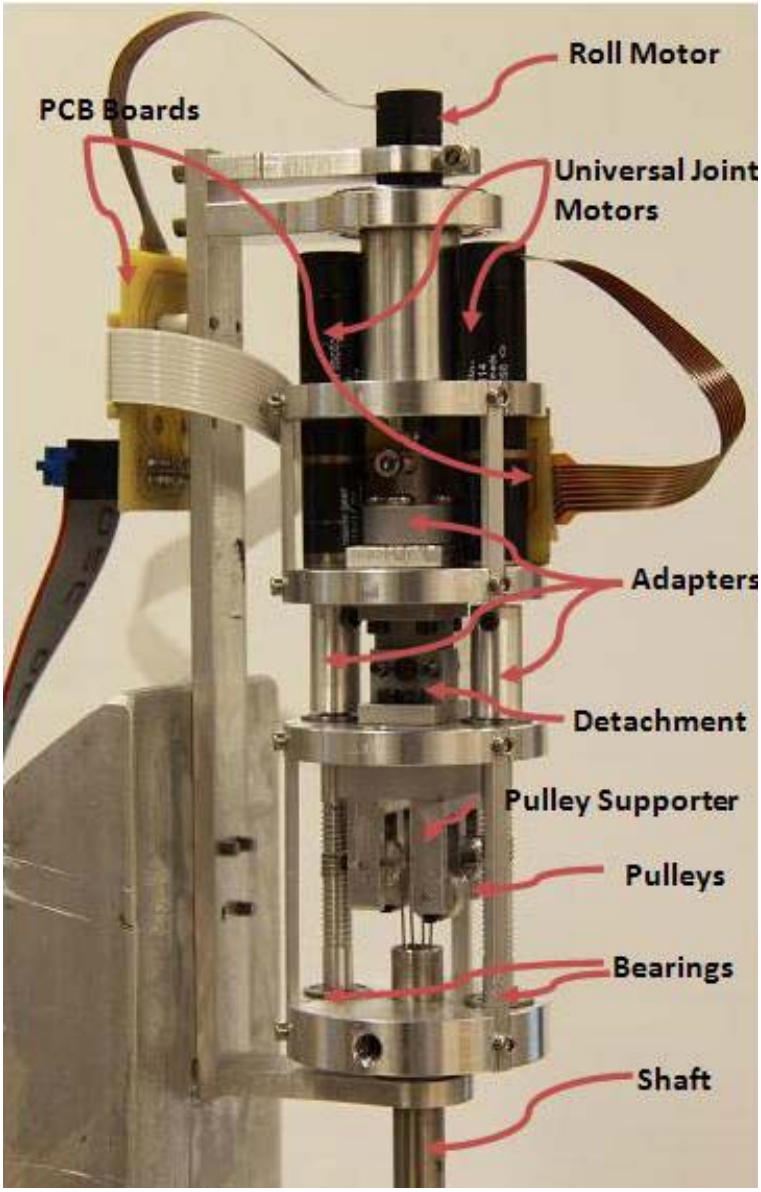

Figure 4.13: Actuation unit prototype

placed on the sides of the roll motor. The diameter of actuation unit is 40 mm. Two slender and long adapters with outer threads are respectively mounted on the shafts of the motors. As it can be seen from the figure, the pulleys are mounted on the pulley supports and the cable is on the pulleys and the adapters. The cable goes around the threads on the adapters and goes through the shaft to the wrist and come back to go by the pulleys to form a closed loop. Two motors use this closed cable loop to transmit the power to the wrist. There are two PCB circuit boards mounted

on the actuation unit to connect the cables of the motors.

4.2.3 Gripper

Throughout the course of a surgery, a number of different surgical tools may be used depending on tasks being performed. In this thesis, we just concentrate on the needle holder as our surgical tool. Kode [10] in our lab designed a gripper using an integrated hybrid shape memory alloy and DC micromotor actuation scheme. In his design, the DC micromotor was mounted to the gripper and SMA wires were used to strengthen the gripping force. The length of the gripper was 40 mm. Its gripping force was 8 N and the gripper cycle time was 1.8 second. In this prototype, the goal was to develop a simpler and cheaper gripper actuation mechanism, for benchtop testing of the test of the robotic system. As such, the gripper actuation mechanism may not necessarily work in vivo in a clinical setting, with the understanding that a variant of the design of Kode [10] will be adopted in the final system. The design, nevertheless, need to achieve sufficient gripping forces for needle grasping. For convenience of fabrication, the tip from a laparoscopic in line needle holder (Summit TR7202 Needle Holder 5mmX35cm, Summit Surgical Technologies, Aurora, Co 80014) shown in Figure 2.3 and Figure 4.14 was cut and integrated as the end-effector. This needle holder has a 5 mm diameter with straight jaw and a Tungsten Carbide tip for holding needle tightly. To shorten the length of gripper and decrease the weight, the actuator was moved out of the gripper to ground and connected by a cable transmission.

4.2.3.1 Mechanical Structure of Gripper

The mechanical structure of the gripper is illustrated in Figure 4.15. The inside dimension of the tip in the figure may be not exactly precise. They are estimated according to outer dimensions. The cross-section of the gripper shown in Figure 4.16 just illustrates the work principle of gripper and should not be measured for accurate calculations.

As it can be seen in the cross-section figure of the gripper, the upper jaw is connected with a shaft and link mechanism to the actuation. A housing covers the end of the gripper and is attached to gripper with two 0-80 set screws. A 115 lbs thrust linear actuator (Part Number HDA2.00-.50, Servocity), located on the ground is used to actuate the gripper. Force transmission from actuator to gripper is supplied by flexible transmission, which includes a 0.018 in diameter, 7×3 stainless steel cable (Part number 3458T86, McMASTER-CARR, Aurora, OH) running through Abrasion-Resistant White ETFE tubing (Part number 5583K41, McMASTER-CARR, Aurora, OH). The cable is tied to the end of the gripper shaft and goes through a tiny hole on the center of the housing's bottom and also fastened to the end of the shaft of a linear actuator. This tubing is not biocompatible and will need to be replaced by a biocompatible material, if the mechanism needs to be used in vivo. In the housing, a soft compression spring (Part Number 9435K22, McMASTER-CARR, Aurora, OH) is placed between the bottom of the housing and a nut mounted on the shaft of gripper. This spring is intended for opening the gripper. Two holders shown in figure 4.16 will clamp the gripper to the instrument by screwing together. These two holders are mounted on the bottom of F/T sensor.

4.2.3.2 Gripper Actuation

The gripper has only 1 DOF and just two simple stages for gripper actuation, closing and opening. In the current design, an off-the-shelf linear actuator is used to actuate

Figure 4.14: Tip of Summit TR7202 Needle Holder

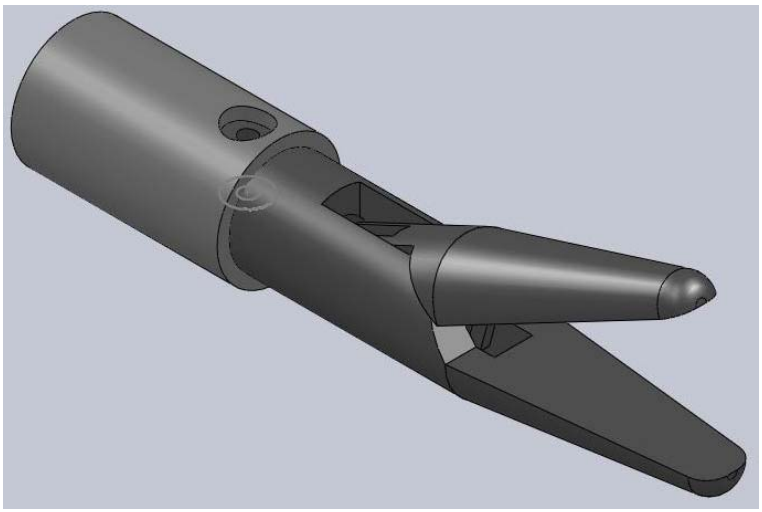

Figure 4.15: Schematic of gripper

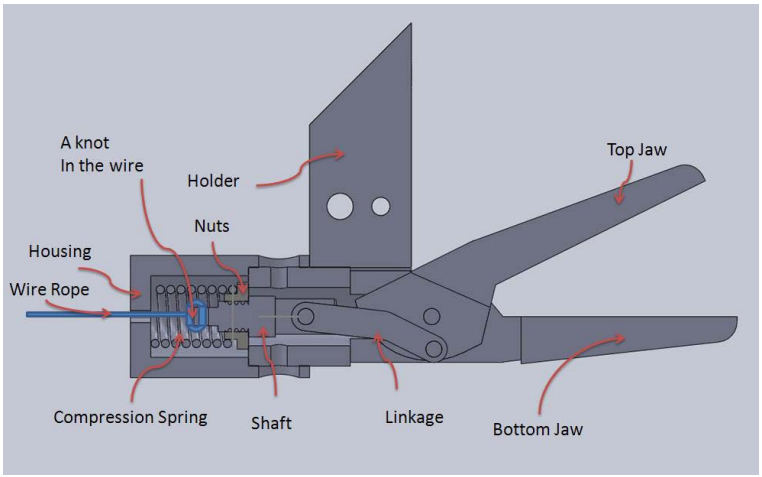

Figure 4.16: Schematic of gripper actuation

the gripper. As this actuator is located at the robot base, size is not a major concern. The operation principle of the gripper is as follows:

The closing action of the needle holder jaw is shown in Figure 4.17. In the figure, the shaft of the linear actuator moves backward and pulls the wire rope, leading to the leftward movements of the shaft and the link of the tip. Consequently the upper jaw will rotate clockwise until it touches the lower jaw tightly. At the same time, the nut on the shaft of the tip will compress the spring backward as well. Although the stroke of the gripper is only 1 mm, due to the flexibility of the cable and the tubing,

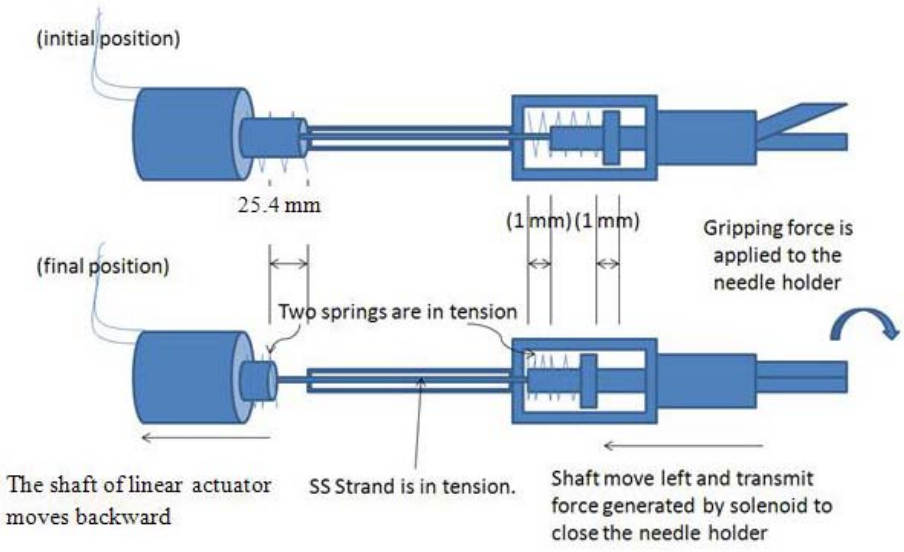

Figure 4.17: Schematic of closing gripper

the stroke for linear actuator is 12 mm, within the stroke range of linear actuator.

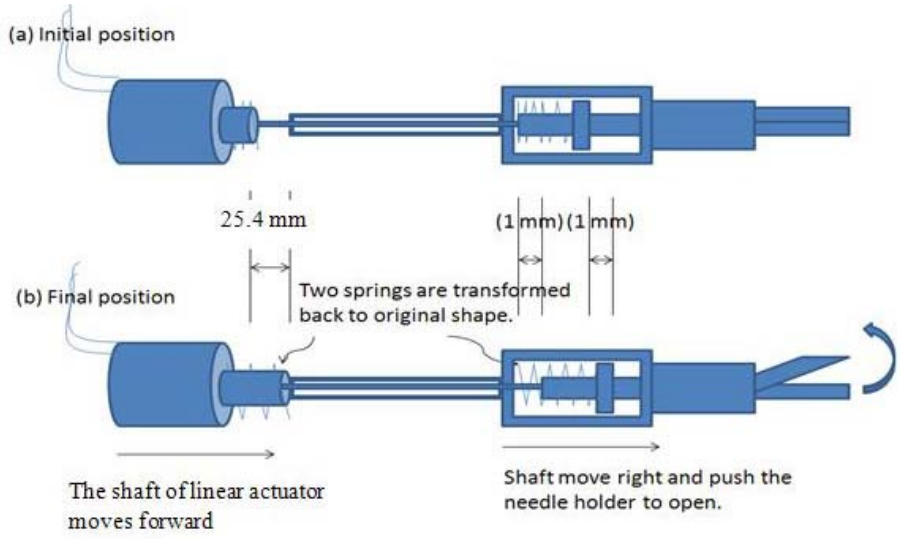

Figure 4.18: Schematic of opening gripper

The opening action of needle holder jaw is shown in Figure 4.18. As seen in the figure, the shaft of linear actuator moves forward, releasing the tension of the wire rope. Consequently the compressed spring propels the shaft and linkage of the gripper back to original position, meanwhile, the linkage drives the upper jaw to rotate counter clockwise to open the gripper.

4.2.3.3 Current Prototype of Gripper

The prototype of gripper is shown in Figure 4.19. The diameter of the gripper is 6.10 mm, the length is 32.30 mm and the weight is 7.3 g. The gripper is clamped by the holders mounted on the F/T sensor. The gripper mechanism can be easily replaced by unfastening the clamps. The gripper makes a 45^o angle with the shaft and the force/torque sensor for ease of operation, by reducing the wrist to gripper distance.

Figure 4.19: Prototype of gripper

4.2.4 Detachment

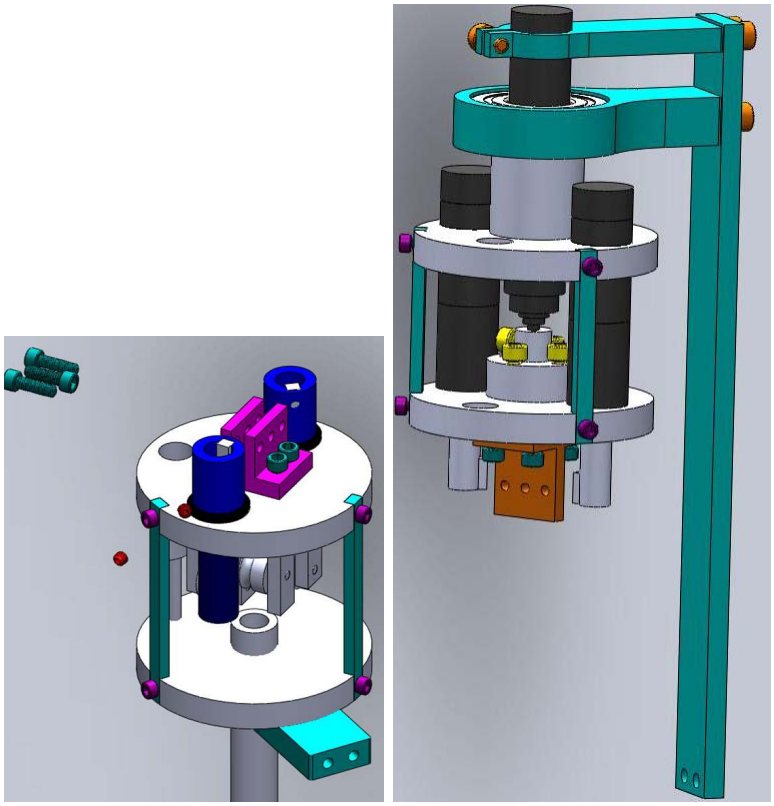

Figure 4.20: ***Left***: Schematic of detachment part 1, ***Right***: Schematic of detachment part 2

The sterilization of the instrument is at high importance. In the operation rooms, every surgical tool is required to be sterilized. The proposed design is intended to be reusable after sterilization. In general, surgical instruments entering the human body must be sterilized to a high sterility assurance level. Usually they are sterilized in autoclave under high pressure steam at 121^{o}C or higher. The motors in the actuation unit are not suitable for sterilization by high temperature and pressure. Because the maximum permissible winding temperature for Maxon RE 10 motors is $+85^{o}$C. Therefore, the instrument has been designed such that the actuation unit does not actually need to be sterilized in autoclave as this unit does not need enter the human body. This is achieved by designing a detachment mechanism to detach the components that would be subjected to sterilization in autoclave from actuation

unit. The two parts after separation are shown in Figure 4.20. The detachment is achieved by just unscrewing five screws. The actuation unit could be wrapped by sterilized plastic bag during surgery and, if necessary, sterilized by other sterilization method after surgery, such as gas plasma.

4.3 Description of Prototype's Electrical Hardware Components

In order to drive the prototype, three Maxon RE 10 motors (Part Number 256105) with built-in encoders are used. Three Maxon LSC 30/2 4-Q-DC servoamplifiers are used to drive these motors. Additionally, with the aim of outputting desired current from amplifier to motor, a Measurement Computing PCI-DDA08/12 board, with 8-channel, 12 bit analog output and 48 bits digital I/O is chosen to control signals to the amplifiers. The digital signals on the PCI-DDA08/12 are used to control emergency software switches. A National Instruments PCI-6602 counter board is used to count position signals from encoders to measure accurate rotating angles of motors. Furthermore, one PCB board to connect PC boards with amplifiers and another board to connect encoders with amplifiers were designed. These components are discussed in Appendix A.

4.4 Control Design

The next step of the prototype design is the design of the motion controllers. The following subsections present the wrist and gripper controller designs.

4.4.1 Wrist Motion Control

In this prototype, the wrist motions are controlled using a joint level proportional-integral-derivative (PID) control scheme, a method widely used in control systems.

The flow chart of the position control of the wrist motors is illustrated in Figure 4.21.

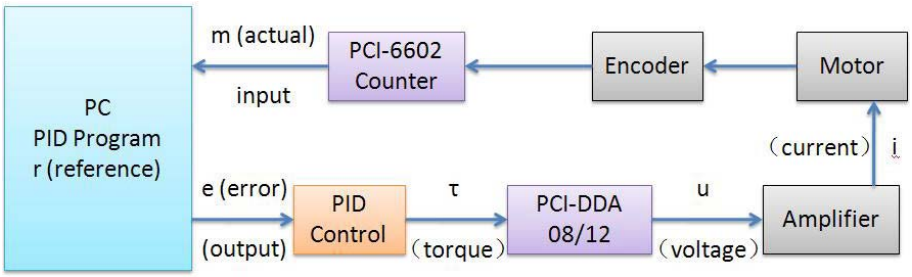

Figure 4.21: Flow chart of position control of Maxon motors

As discussed in section 4.3, the input-output relationship of the motor-amplifier are in the form:

$$U = aI + b \tag{4.28}$$

where a and b are experiment determined coefficients, U represents analog voltage input, and I represents analog current output.

For DC motor, there is a linear relationship between torque τ and current I characterized by a torque constant K:

$$\tau = KI. \tag{4.29}$$

Consequently, we can obtain

$$U = a \cdot \tau / K + b \tag{4.30}$$

by substituting equation (4.29) into equation (4.28).

Equation of error, $e = (r - m)$, where e represents error, r represents reference position, and m represents actual position measured from encoder, is shown in Figure 4.22. By using PID control, we intend to minimize the error to a minimum values by selecting the proportional, the integral and derivative values, K_p, K_i, K_d respectively and appropriately. From the Figure 4.22, equation of torque

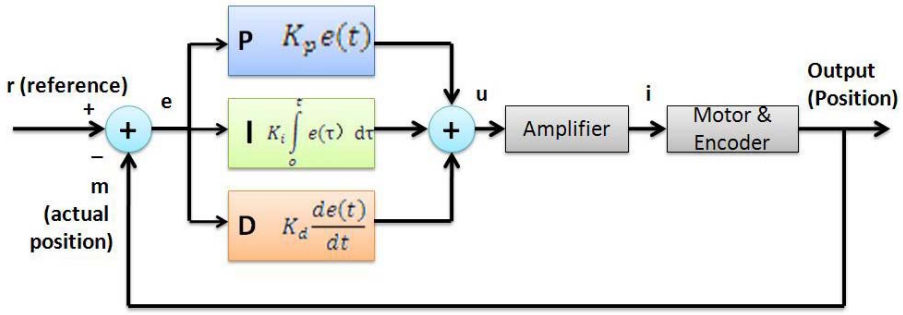

Figure 4.22: Flow chart of PID control of Maxon motors

$$\tau = K_p e(t) + K_i \int e(\tau) d\tau + K_d \frac{de(t)}{dt} \tag{4.31}$$

can be derived based on principle of PID control. Finally, we get the equation of voltage for amplifier by substituting equation (4.31) into equation (4.30)

$$U = a(\frac{K_p e(t) + K_i \int e(\tau) d\tau + K_d \frac{de(t)}{dt}}{K}) + b, \tag{4.32}$$

where, $e = (r - m)$.

The PID controller was implemented using LabView software (National Instrument,Austin, TX 78759-3504).

4.4.2 Gripper Control

The gripper actuation is controlled using a PD controller. The flow chart of PD position control of linear actuator is shown in Figure 4.23 and is similar to Figure 4.21. NI DAQPad-6015 obtains the position of the linear actuator in real-time using the integrated potentiometer. By PD control, the error between the reference position and actual position of linear actuator is converted to a voltage value. Then the NI DAQPad-6015 outputs this voltage to Maxon LSC 30/2 Amplifier, which drives the linear actuator.

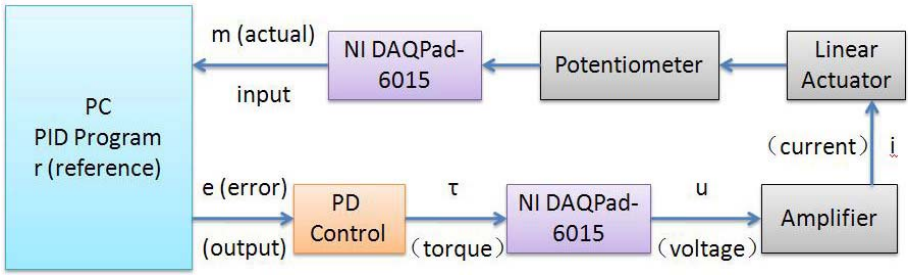

Figure 4.23: Flow chart of position control of linear actuator

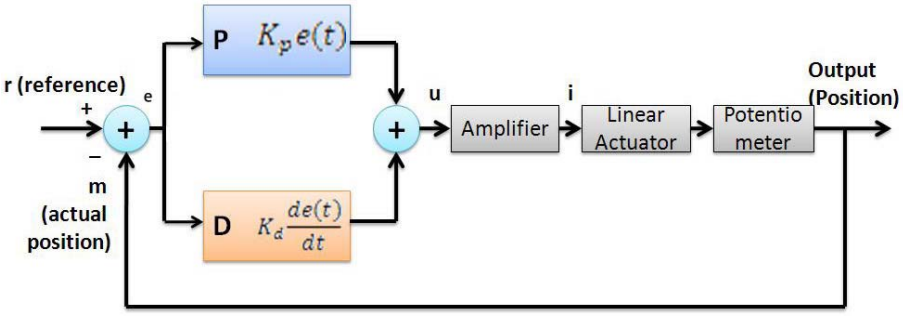

Figure 4.24: Flow chart of PD control of linear actuator

Chapter 5

Test Results of the Prototype

In this chapter, the results of the tests performed to evaluate the constructed prototype is presented.

5.1 Test Results of Wrist

5.1.1 Range of Motion

The first test performed was to evaluate the range of motion of the individual joints of the wrist. Using the position controller with 200 Hz sampling rate, the same reference angular positions were input to both wrist motors and incrementally increased at 1^o steps, resulting pitch motion. The results showed that the wrist can pitch about axis 1 by $\pm 90°$. Then, reference angular positions in opposite directions were applied, leading to yaw motion, and also incrementally increased at 1^o steps. The results showed that the wrist can yaw about axis 2 by $\pm 35°$. The roll axis was also similarly tested, which showed that the instrument can roll about axis 0 by $\pm 360°$, as shown in Figure 5.1.

Figure 5.1: Schematic of 3 DOF motions

5.1.2 Speed of Motion

The second test performed was to evaluate the speed of motion of the wrist joint. Using the PD controller described in Section 4.4, the prototype's roll motion was actuated to rotate to any desired position. The test showed that rolling from $-360°$ to $360°$ took 1 s. In other words, the speed of roll motion was $720°$/sec. The speeds of the other wrist joints were tested using a similar procedure. The results showed that, the wrist pitched from 0 to $45°$ in approximately 0.5 s and yawed from 0 to $30°$ in approximately 0.5 s. Hence, the maximum angular velocities were identified as $90°$/s and $60°$/s for the pitch and yaw axes.

5.1.3 Test Wrist Rotation

The third test performed was to evaluate the performance of wrist rotation. Rotating a circle around the central point of wrist was chosen as the target wrist motion. Polaris Vicra optical sensor (NDI, Northern Digital Inc, Waterloo, Ontario, Canada)

was used to track the trajectory of wrist's central point. Using the position controller with 154 Hz sampling rate, the reference angular positions were input to both wrist motors. The 2d trajectory of wrist rotation is shown in Figure 5.2 and 3d trajectory is shown in Figure 5.3.

Based on forward kinematics of instrument and the mapping from motor angles to wrist angles presented in Section 4.1.1, using the reference angular positions, the desired trajectory is the red circle shown in Figure 5.2. The blue trajectory is drawn based on actual angular data from encoders. The black trajectory in dash line is recorded by optical sensor.

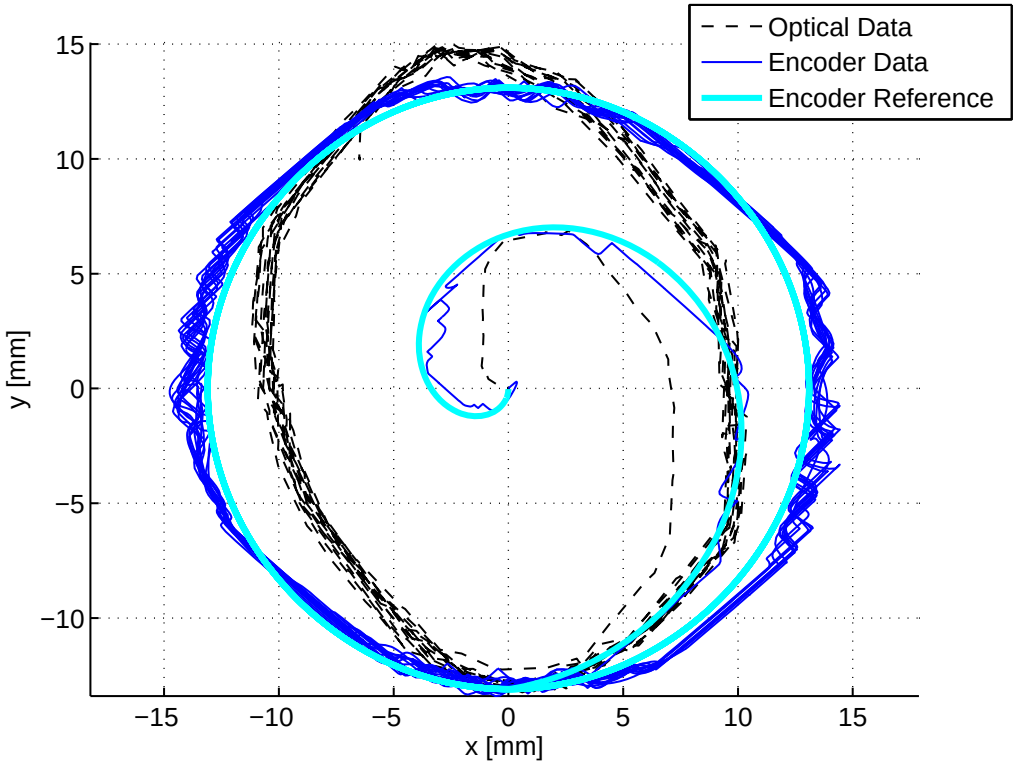

Figure 5.2: 2D trajectory of wrist rotation

5.1.4 Test Force and Torque

The next test performed was to measure the force capabilities of the wrist joints. An ATI 6 axis force/torque sensor (Type SI-25-0.25) was used to measure the forces and

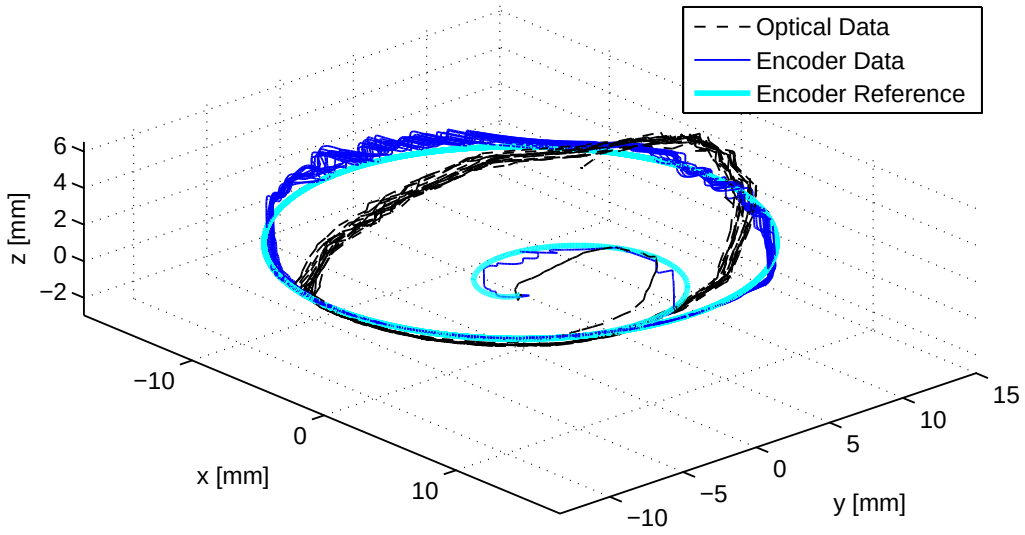

Figure 5.3: 3D trajectory of wrist rotation

torques of the instrument. The specifications of this sensor is shown in Table 5.1.

Table 5.1: Specification of force/torque sensor

Sensing Ranges				Resolution			
Fx, Fy	Fz	Tx, Ty	Tz	Fx, Fy	Fz	Tx, Ty	Tz
25N	35N	250Nmm	250Nmm	1/160N	1/160N	1/32Nmm	1/32Nmm

The experiment setup was the same with the one shown in Figure 4.7. The instrument was fixed to a metal piece with a screw and the sensor was mounted on the wrist attachment. A plastic piece was fixed next to the sensor to prevent wrist motion, so that blocking forces can be measured. For wrist to be in static equilibrium, the sum of the torques about any point must be zero. The equation of the sum of the torques at the center of wrist joints is given as:

$$\sum \tau = \tau_w + \tau_s = 0, \tag{5.1}$$

where τ_w represents the wrist joint torques and τ_s represents the torques measured

by force/torque sensor. Moving τ_s to the left side of equation (5.1) yields

$$\tau_w = -\tau_s. \tag{5.2}$$

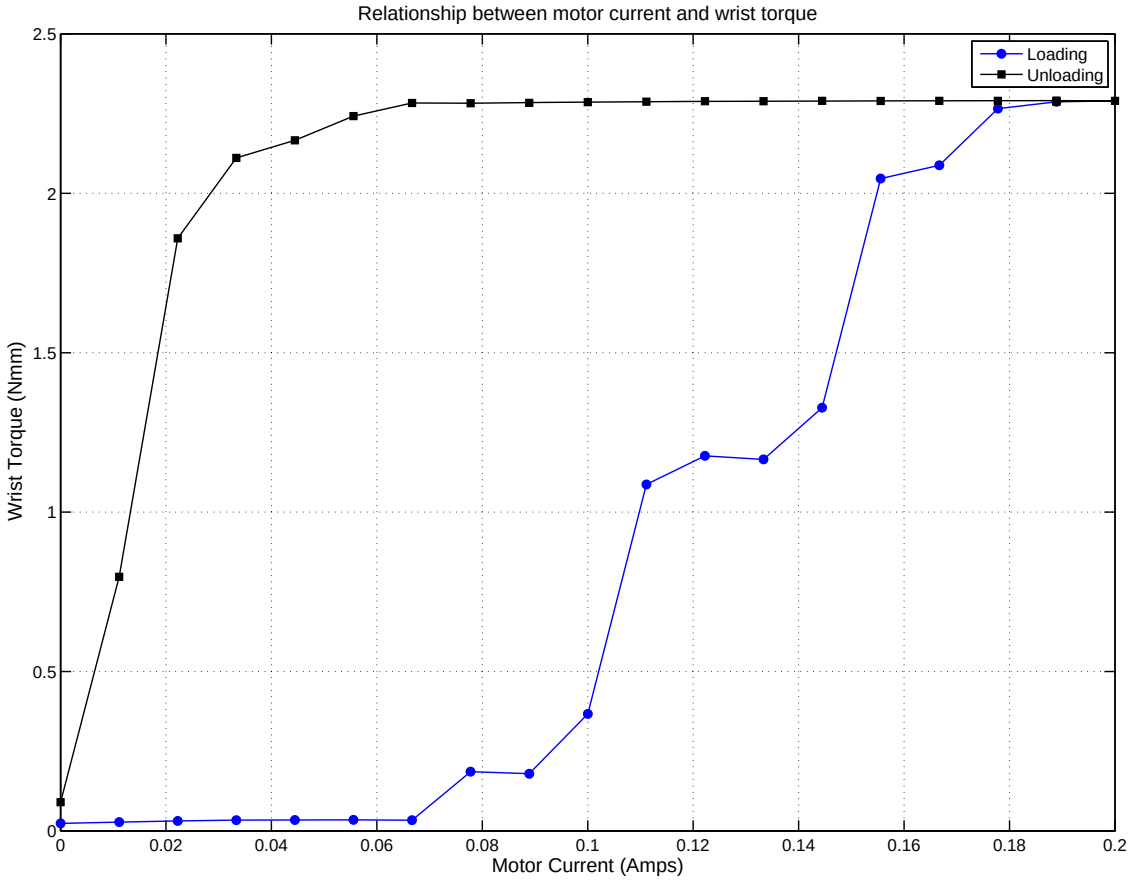

Figure 5.4: Experiment result of relationship between motor current and wrist torque (yaw motion)

So the torque value of wrist equals the torque value measured by sensor, but in the opposite direction. For yaw motion, opposite torques were applied to both motors and incrementally increased the motor torque at 0.1 Nmm starting from 0 to 1.8 Nmm, and then decrementally decreased the motor torque at 0.1 Nmm starting from 1.8 Nmm to 0. Then torque values measured by the sensor (i.e. wrist joint torque) were recorded as shown in Figure 5.4. For pitch motion, same torques were applied to

both motors and the motor torques were incrementally increased at 0.1 Nmm steps starting from 0 to 1.8 Nmm, and then decrementally decreased the motor torque at 0.1 Nmm starting from 1.8 Nmm to 0. Then the torque values measured by the sensor (i.e. wrist joint torque) were recorded as shown in Figure 5.5.

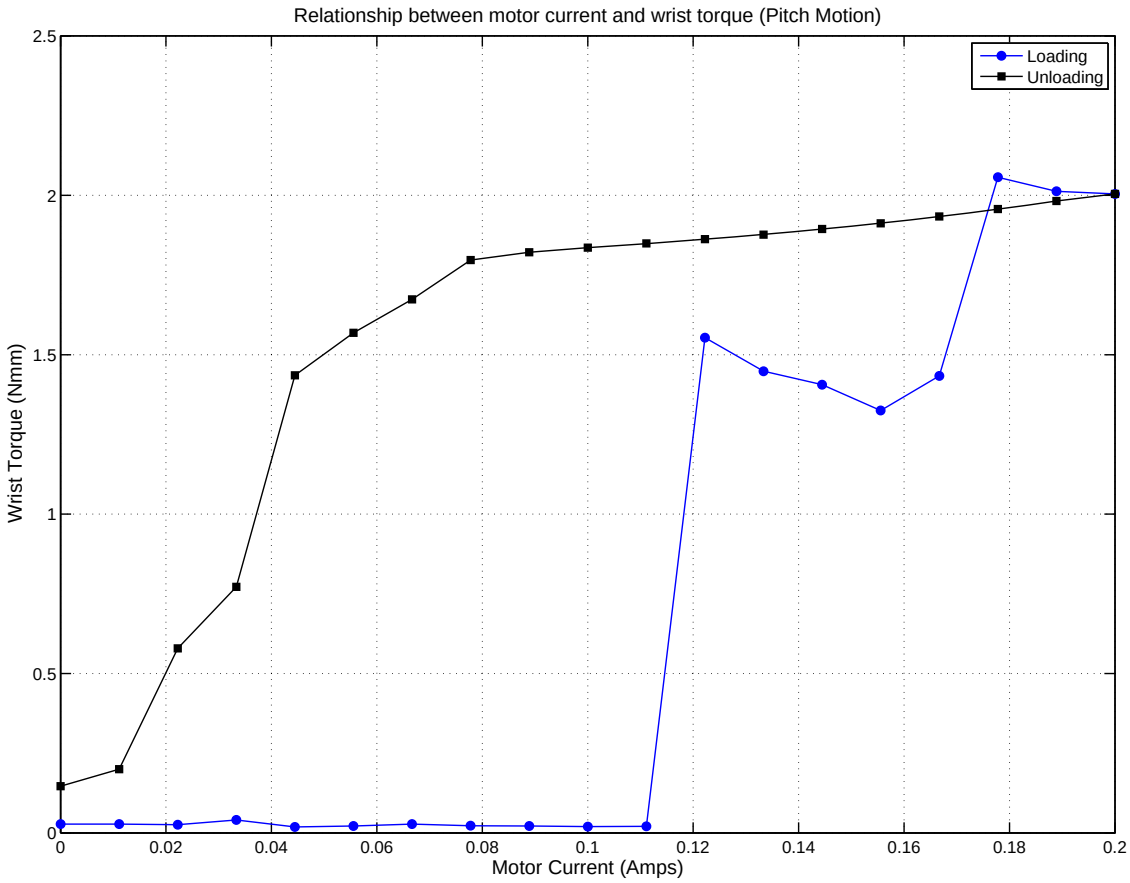

Figure 5.5: Experiment result of relationship between motor current and wrist torque (pitch motion)

5.1.5 Discussion

As it can be seen in Figure 5.2, the blue trajectory based on actual angular positions from encoders is not smooth. One possible reason is that due to the limitation of the operating system used in implementation of the control algorithms, the sampling rates

of the control program could not be improved, which limited the control performance. In the future, if the control program can be implemented using a real-time operating system, such as XPC, the instrument would perform better. Additionally, there is a gap between trajectory of wrist rotation and desired trajectory, the black trajectory and red one shown in Figure 5.2. This problem could be caused by the rubbing of the cable inside shaft, which increased the friction. Another possible reason is tendon slipping, which was observed on the wrist's pulleys while the wrist was rotating. The reason of this problem is that the friction between the cable and the pulleys are too small. In order to increase the friction to reduce slipping, the cable was wrapped around the pulleys one more loop, which increased the contact surface between the cable and pulley. Another way to reduce slipping would be to increase the tension on the cable to increase the friction. However, the increased friction would increase the load on the actuators and potentially reduce the performance of instrument. So the balance between the friction and performance should be determined based on a series of experiments.

The result of wrist torque shown in Figure 5.5 and 5.4 showed that the actuation power from motors is lost drastically during tendon transmission through the 8 mm diameter instrument shaft. One possible reason of this is the rubbing of the cable inside shaft. If more forces at the needle tip are desired, cable guide plates can be used to prevent rubbing.

5.2 Test Results of Gripper

5.2.1 Gripping Force

The aim of this experiment is to test the gripping force of the gripper, which is defined as the force to clamp needle exerted by gripper's jaws, perpendicular to the surface of jaws. A 0-90 N force gauge (AccuForce, Mansfield and Green Division of AMETEK) is used to measure gripping force. The experiment setup is shown in Figure 5.6. Force

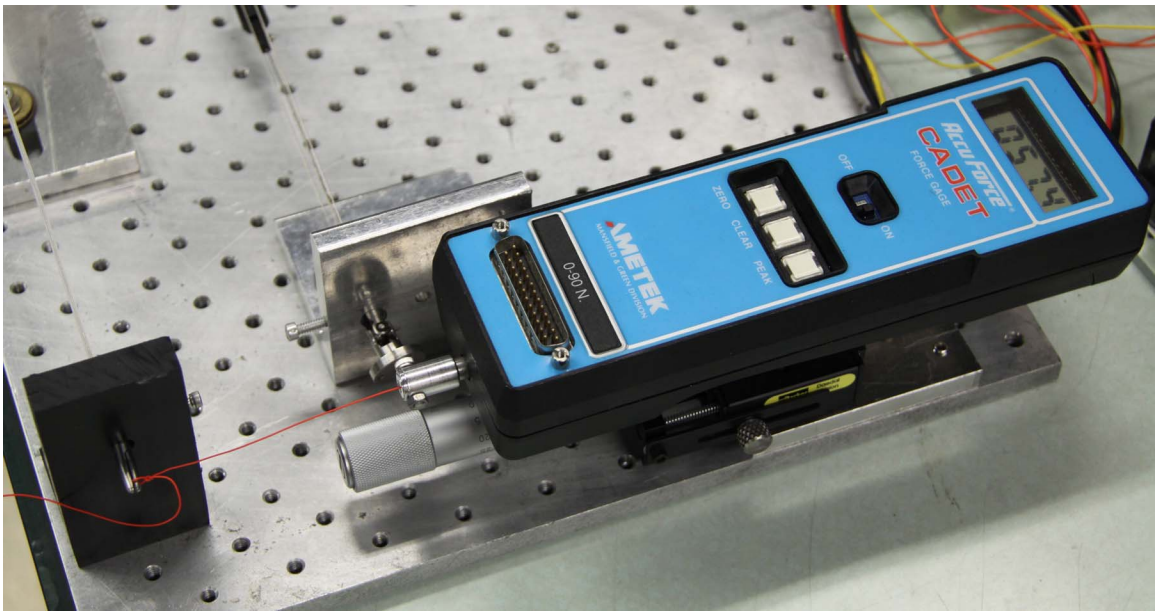

Figure 5.6: Experiment setup of measuring gripping force of gripper

gauge is mounted on a 1.75" single axis translation stage (Edmund Optics), which can move linearly. The gripper is tightly fixed with a screw in a support piece. A wire is connected between the tip of force gauge and the upper jaw of gripper. There are two ways to measure gripping force. One way is that when the gripper is closed by the pulling of actuator, the gauge is moved backward with translation stage until the upper jaw opens. Another way is to keep the gauge still, then actuate the actuator to try to close the jaw.

In this test, two positions were chosen to place the needle. To simplify naming convention of these positions, they were called as position 1 and position 2, as shown in Figure 5.7. The length of jaw was defined as L. The fourth line from left to right in the figure represents 0 position and the first line represents a position away from 0 position at a distance of L. So position 1 was located on a position from 0 a distance of 0.75L and position 2 was placed on a position from 0 a distance of 0.5L.

At the first, the gripping force of the TR7202 needle holder, which is used in MIS, was tested. The needle was placed on position 1, as shown in Figure 5.7. There were four clamping positions on this needle holder. The results of the gripping forces

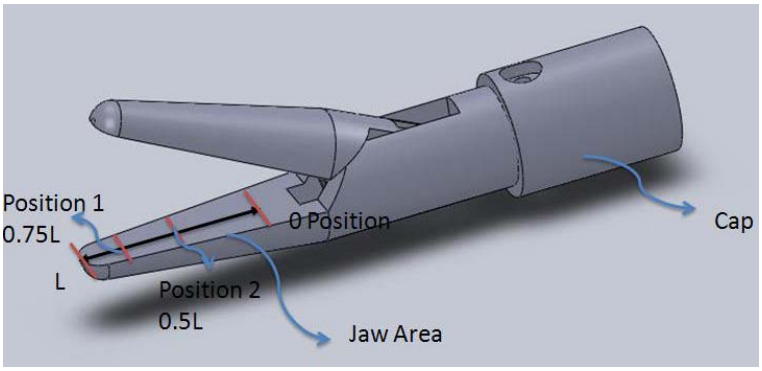

Figure 5.7: Schematics of needle's positions in gripper

Table 5.2: TR7202 needle holder's performances

Level	Gripping force
1	26.8 N
2	45.8 N
3	64.0 N
4	80.0 N

versus clamping positions were given in Table 5.2. Then a performance test for suturing actions using this needle holder and a curved needle placed on position 1 was conducted using a phantom tissue [12], a square sample of silicone rubber (RTV 6186, Momentive) with behavior similar to soft tissues. This test was performed by the needle holder with 26.8 N gripping force. The experiment result showed that exerted 26.8 N gripping force on the curved needle, the needle insertion into this phantom tissue could be completed successfully.

A linear actuator (Part number HDA2.00-.50, Servocity) was used to actuate the gripper. The maximum thrust force of actuator is 511.5N (115 lbs.) at 12 Volts. Force transmission between the gripper and the linear actuator was supplied by a flexible transmission, which is composed of a stainless steel wire and a plastic tubing. Because of the size of the gripper, there are limited choices for stainless steel wire selection. The diameter of the wire cannot be larger than 0.020". This restriction limited the choices for the tubing. Initial tests with the available tubing failed due to large forces provided by the actuator. The ends of the tubing (Part Number

Table 5.3: Specifications of tubing

Tubing Type	Inside Diameter	Outside Diameter	Hardness
Silicone rubber	0.0625”	0.292”	60A (Shore A)
High-pressure nylon	0.073”	0.125”	108 (Rockwell R)
Nylon vacuum	0.078”	0.125”	112 (Rockwell R)
White ETFE	0.020”	0.0625”	63D-72D (Shore D)

5583K42, McMASTER-CARR, Aurora, OH) mentioned in subsection 4.2.3.1 were damaged due to its thin wall thickness. Since tubing with larger wall thickness were not available, a larger tubing was used to reinforce the small diameter tubing by inserting the small tubing into the larger one. Three kinds of outer tubing were chosen for testing with the inner tubing. These are high-purity white silicone rubber tubing (Part number 51735K21, McMASTER-CARR, Aurora, OH), high-pressure white Nylon 11 tubing (Part number 9685T103, McMASTER-CARR, Aurora, OH) and Nylon Vacuum tubing (Part number 5173K914, McMASTER-CARR, Aurora, OH). The specifications of these tubing are listed in Table 5.3.

Experiments showed that this solution can solve the problem and gripper can open smoothly. Although all three of the tested tubing attained the goal of smooth gripper operation, the performances were different. The two hard tubing suffered some minor deformation. Due to softness of material and braid-reinforced structure, silicone rubber tubing can absorb the deformation by transforming itself. But this tubing was heaviest and biggest among them. Therefore, White ETFE Tubing as inner tubing and High-pressure Nylon tubing as outer tubing were chosen for flexible transmission because this outer tubing not only can facilitate smooth opening, but it is also lightweight and smaller in diameter.

One important effect observed was the reduction of the gripping force, when the flexible transmission with double tubing is used. In order to identify the source of the gripping force reduction, gripping force under flexible transmission mentioned above, direct non-flexible transmission but with gripper cap and springs, and finally, direct

non-flexible transmission without the cap and spring were compared. The experiment results are shown in Table 5.4.

Table 5.4: Performance of gripping force at two positions with different conditions

Condition	At position 1		At position 2	
	Backdriving Force(N)	Gripping Force(N)	Backdriving Force(N)	Gripping Force(N)
Cap, spring and tubing	3.5	3.7	5.5	7.9
Cap and spring without tubing	9	10	10.6	12.1
Without tubing, cap or spring	11.8	11.4	13.4	14

Both position 1 and position 2 were tested for a comparison. Since position 2 was closer to the pivot of gripper, the force on position 2 was larger than the force on position 1, as expected. With and without cap, the differences of gripping force were about 1.4 N and 1.9 N at the two positions. This demonstrates that the spring (Part Number 9435K22, McMASTER-CARR, Aurora, OH) in the cap and friction produced by wire going through the hole was responsible for some part of the gripping force loss. A substantial loss in the gripping force was caused by the flexible transmission. In the tests, the tubing became bumpy when the gripper was in the closed position. We conjecture that friction, caused by the contact between wire and tubing, was main reason of the substantial ripping force loss.

5.2.2 Gripper Cycle-time

The purpose of the last test was to measure the opening-closing times, and the cycle-time of the gripper. The opening and closing times of the gripper were measured to be 3 s each. Although this operation time is not fast enough for actual surgery, it is sufficient for in lab use. The reason of the slow motion is the speed of linear actuator, which is only 0.5 in/s at 12 volts.

Chapter 6

Conclusion

6.1 Summary

This thesis presents a three DOF robotic wrist mechanism with force feedback for a robotic surgery system. This prototype solves the problem of limited dexterity of traditional surgical tools in MIS caused by small incision acting as a fulcrum. The prototype improves dexterity by integrating a 2 DOF wrist on the instrument tip. Another problem of the current surgical tools in MIS is that they cannot provide force feedback from the instrument/tissue interaction. Integrated with a 6 axis force/torque sensor, the designed instrument can provide accurate force and torque measurements on the instrument tip during instrument/tissue interaction. The shaft has an 8 mm diameter shaft. The 3 DOF instrument can roll $\pm 360^o$, pitch $\pm 90^o$, and yaw $\pm 35^o$, hence the workspace of the end-effector is a semisphere. The gripper can provide 5.5 N gripping force. The diameter of the gripper is approximately 6.10 mm, its length is 32.3 mm and it weights 7.3 g. The angle of gripper jaw opening is 45^o. The end-effector can be easily replaced by different surgical tools depending on task being performed.

6.2 Future Work and Improvements

The dexterity of the universal joint could still be improved. As mentioned earlier, yaw motion can only extend to $\pm 35^o$ due to physical limitations of the universal joint, which restricts dexterity of the wrist motion. One option to improve the range of the wrist motion is to assemble two universal joints together, so that pitch motion of the wrist can be reached approximately $\pm 180^o$ and yaw motion can be extended to $\pm 70^o$. This solution drastically extends the workspace of the wrist and noticeably increases its dexterity.

The current gripper still needs to be improved to be used in *in vivo* studies. Gripping force could be increased by incorporating a mechanical gain mechanism, such as lever at the end of gripper. Additionally, once the gripping force is increased to reach the requirements, replacing the linear actuator with a faster actuator can decrease the cycle-time of the gripper to lower than 1 s. If a custom gripper could be designed, it can decrease the overall length of the end-effector and can increase the amount of gripping force.

The present research was only focused on the design of a 3 DOF instrument with a 2 DOF dexterous wrist mechanism. Future research concentration will be placed on the design of a base manipulator, on which the designed instrument will be mounted. This base manipulator will have 3 active DOF and 2 passive DOF, providing sufficient dexterity to the end-effector and accommodate entry point constraints to complete different surgical task. Once the whole robotic surgery system is set up, the suturing action would be tested on phantom tissues and then in *in vivo* tissues.

Appendix A

Electrical Hardware Components

A.1 Amplifiers

The LSC 30/2 is a linear 4-Q-Servoamplifier. The supply voltage is 12-30 VDC and the maximum output current is 2 A. Current control was chosen as the operating mode of the amplifiers and input set value range from -10 V to 10 V. Input and output pinouts of the amplifier is shown in Table A.1. There are totally four servoamplifiers, including amplifier 0 for roll motor, amplifier 1 and 2 for universal joint, and amplifier 3 for linear actuator.

For every amplifier, it is valuable to model the linear relationship of input voltage and output current. A National Instruments PCI-6221 board was used to characterize the input-output of the amplifier. Input voltage of the amplifier were set to discrete values of 0V, 0.5V, 1V,1.5V,2V, 3V, 4V, 5V and -0.5V, -1V, -1.5V, -2V, -3V, -4V, -5V. A Maxon RE-10 DC motor (♯118383)with GP-10A Gear Head (♯218415) was selected as a load. In addition, the motor's shaft was kept stationary while it was working. While the currents corresponding to the voltages from "+motor" and "-motor" outputs on the amplifier were measured and recorded.

Table A.1: Pinout of Amplifier

Pin Number	output
1	+Motor
2	-Motor
3	+Vcc
4	Gnd
5	+Vaux
6	-Vaux
7	-Set
8	+Set
9	SigGnd
10	Dis IN
11	Dis +V
12	Ready
13	-T/ChA
14	+T/ChB
15	Gnd
16	+Venc

A.1.1 Amplifier 0 for Roll Motor

The data of current and voltage are shown in Table A.2. And the data are fit in Matlab, as shown in Figure A.1. As it can be seen , the relationship is given by

$$y_0 = 4.5545x_0 + 0.0021, \tag{A.1}$$

where, y_0 represents analog input to amplifier 0 and x_0 represents current output from amplifier 0.

Table A.2: Relationship between voltage and current of amplifier 0

Voltage (V)	Current (mA)
0	0
0.5	110
1	219
1.5	329
2	439
3	658
4	877
5	1096
-0.5	-109
-1	-219
-1.5	-329
-2	-439
-3	-659
-4	-880
-5	-1100

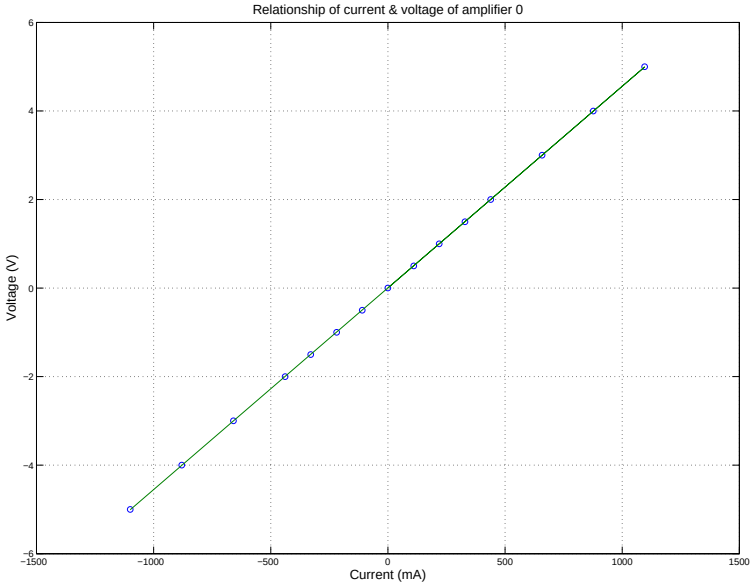

Figure A.1: Schematics of relationship of voltage and current of amplifier 0 fit in Matlab

A.1.2 Amplifier 1 and 2 for Universal Joint

The data of current and voltage of amplifier 1 and amplifier 2 are shown in Table A.3 and Table A.4 respectively. And the data are fit in Matlab, as shown in Figure A.2

Table A.3: Relationship between voltage and current of amplifier 1

Voltage (V)	Current (mA)
0	2.2
0.5	111.7
1	220.7
1.5	329.9
2	440
3	658
4	876
5	1095
-0.5	-105.6
-1	-215.4
-1.5	-325.3
-2	-435
-3	-654
-4	-874
-5	-1094

and A.3. As it can be seen , the relationships are given by

$$if \;\; x_1 \geq 0, \qquad y_1 = 4.5764x_1 - 0.0107, \tag{A.2}$$

$$if \;\; x_1 < 0, \qquad y_1 = 4.5582x_1 - 0.0162, \tag{A.3}$$

$$if \;\; x_2 \geq 0, \qquad y_2 = 4.8512x_1 - 0.0267, \tag{A.4}$$

$$if \;\; x_2 < 0, \qquad y_2 = 5.1101x_2 + 0.1342, \tag{A.5}$$

where, y_1 represents analog input to amplifier 1 and x_1 represents current output from amplifier 1, and y_2 represents analog input to amplifier 2 and x_2 represents current output from amplifier 2.

Table A.4: Relationship between voltage and current of amplifier 2

Voltage (V)	Current (mA)
0	-6.24
0.5	102.8
1	215.0
1.5	321.9
2	434
3	650
4	798
5	1036
-0.5	-115
-1	-226
-1.5	-337
-2	-447
-3	-640
-4	-762
-5	-1004.7

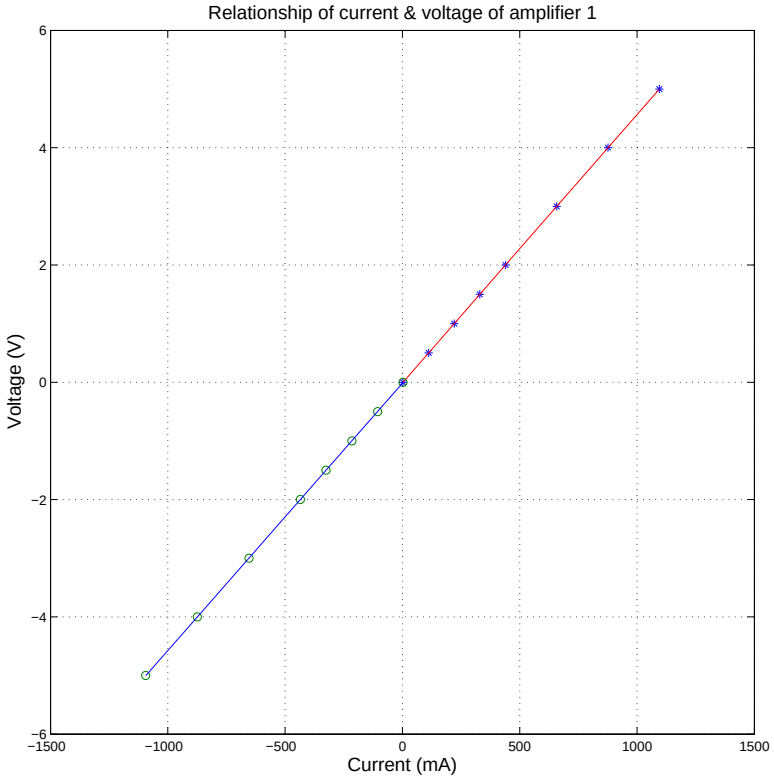

Figure A.2: Schematics of relationship of voltage and current of amplifier 1 fit in Matlab

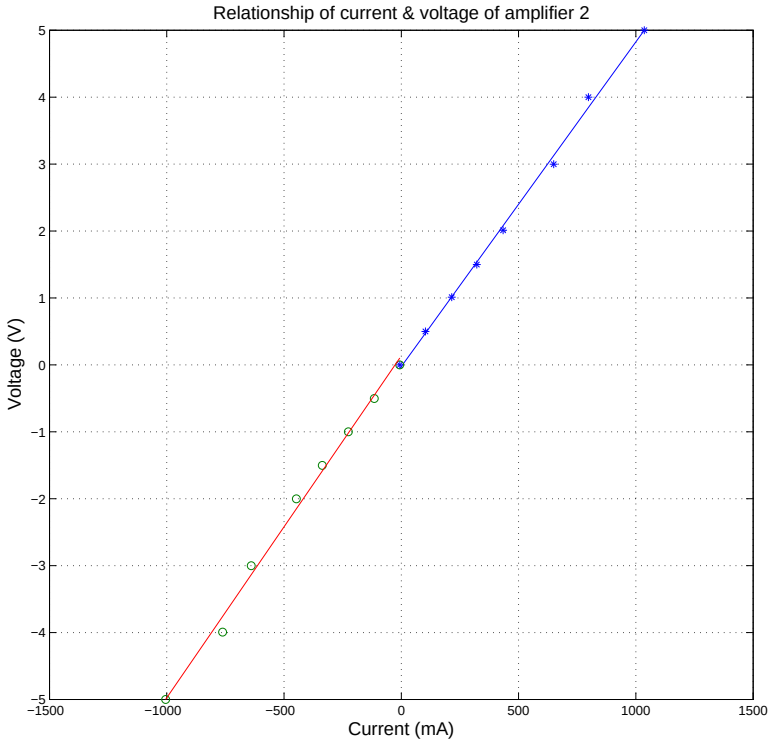

Figure A.3: Schematics of relationship of voltage and current of amplifier 2 fit in Matlab

Table A.5: Relationship between voltage and current of amplifier 3

Voltage (V)	Current (mA)
0	-14.26
0.5	94.0
1	202.4
1.5	310.7
2	420
3	636
4	853
5	1070
-0.5	-122
-1	-231
-1.5	-340
-2	-448
-3	-666
-4	-884
-5	-1101

A.1.3 Amplifier 3 for Linear Actuator

The data of current and voltage are shown in Table A.5. And the data are fit in Matlab, as shown in Figure A.4. As it can be seen , the relationship is given by

$$if \;\; x_3 \geq 0, \qquad y_3 = 4.6114x_3 + 0.0661, \tag{A.6}$$

$$if \;\; x_3 < 0, \qquad y_3 = 4.5981x_3 + 0.0627, \tag{A.7}$$

where, y_3 represents analog input to amplifier 3 and x_3 represents current output from amplifier 3.

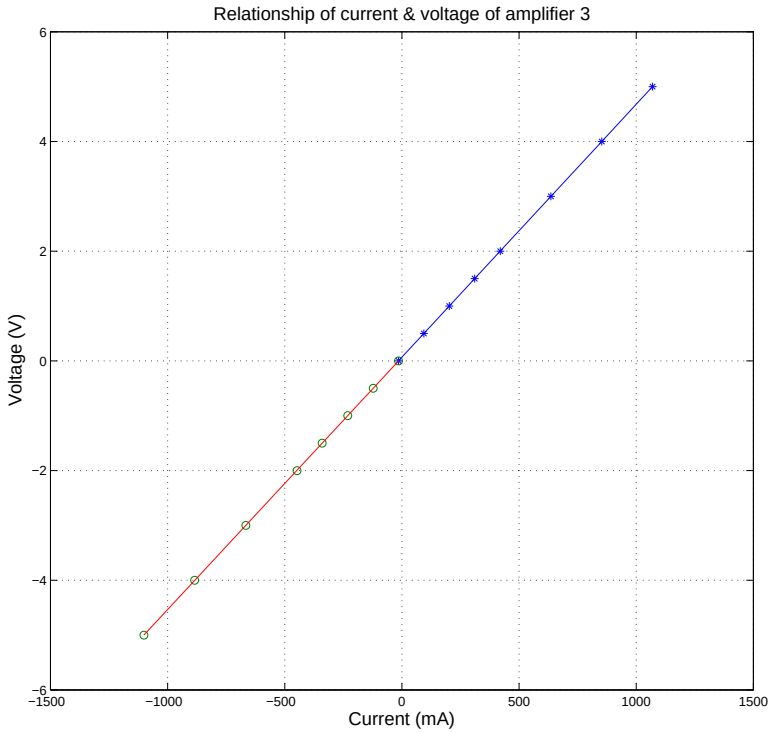

Figure A.4: Schematics of relationship of voltage and current of amplifier 3 fit in Matlab

A.2 Data Acquisition System

For joint position measurements from motor encoders, a National Instruments PCI-6602 boards is used. PCI 6602 is an 8-channel, 32-bit counter/timer board. Connector pinout is shown in figure A.5. Pin 2 “PFI 39/CTR 0 SOURCE” is connected to Channel 0A from encoder for roll motion and Pin 40 “PFI 37/CTR 0 AUX” is connected to Channel 0B from encoder for roll motion. Pin 7 “PFI 35/CTR 1 SOURCE” is connected to Channel 1A from encoder 1 for wrist motion and Pin 6 “PFI 33/CTR 1 AUX” is connected to Channel 1B from encoder 1 for wrist motion. Pin 34 “PFI 31/P0.31/CTR 2 SOURCE” is connected to Channel 2A from encoder 2 for wrist motion and Pin 66 “PFI 29/P0.29/CTR 2 AUX” is connected to Channel 2B from encoder 2 for wrist motion.

For analog outputs to the motors, a Measuring Computing DDA08/12 board is used. DDA08/12 is an 8-channel, 12-bit analog output board with 48 digital I/O lines. It has a 100-pin output. One purpose of this board is to control set values input to amplifiers by PC. Another purpose is to use digital signals as emergency software switches. The connector pinout is shown in Figure A.6. Pin 1 and pin 2 are for “+set” and “-set” of amplifier 1. Pin 3 and pin 4 are for “+set” and “-set” of amplifier 2. Pin 5 and pin 6 are for “+set” and “-set” of amplifier 3. Pin 55 is digital output for roll motion motor. Pin 51 is digital output for motor 1 for wrist motion and pin 52 for motor 2 for wrist motion.

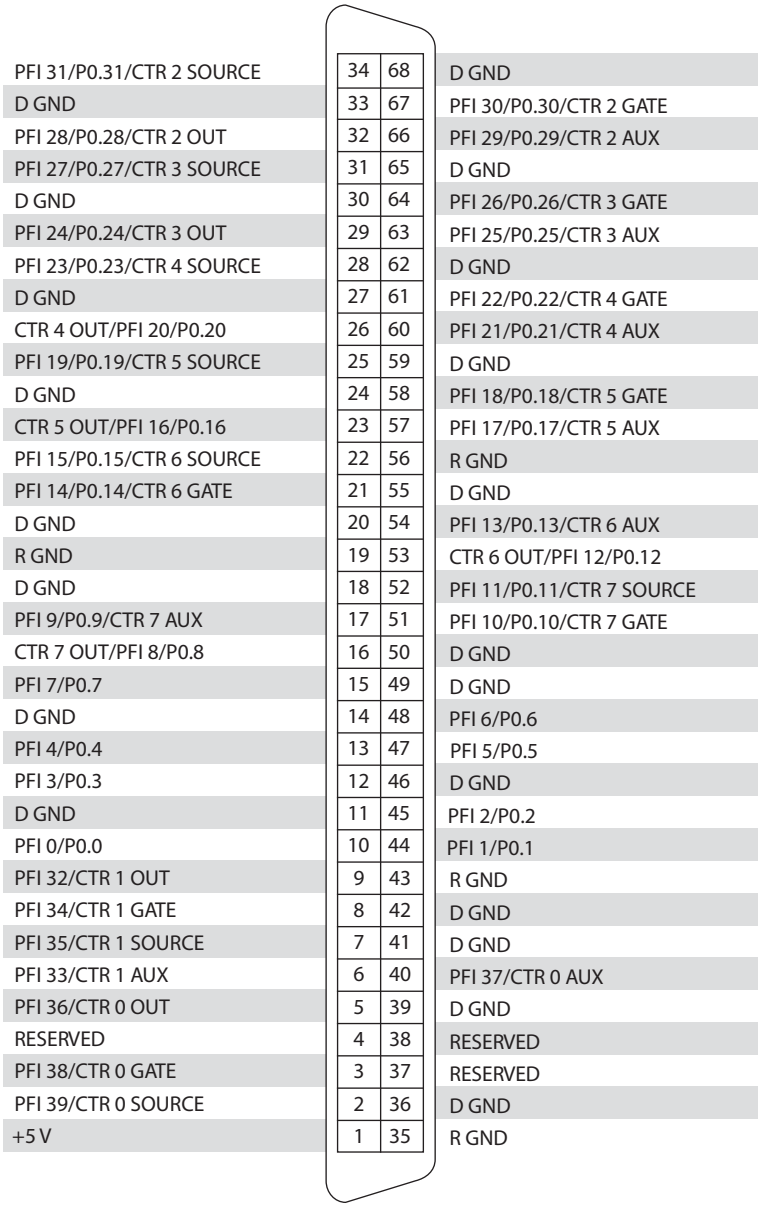

Figure A.5: NI 6602 Connector Pinout

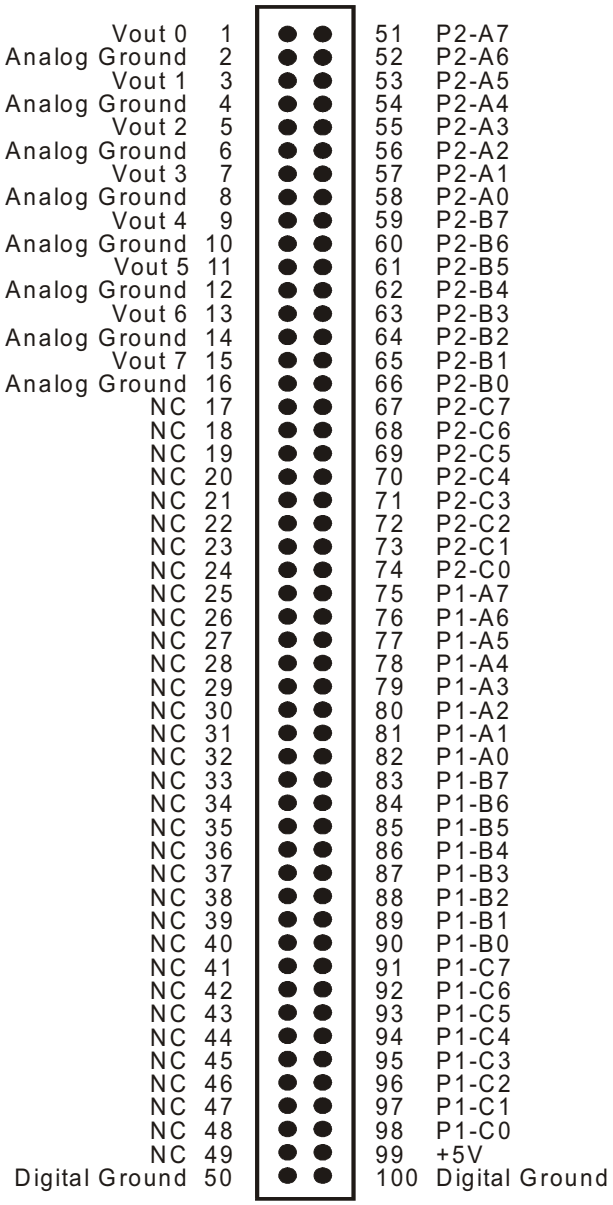

Figure A.6: DDA08/12 Connector Pinout

A.3 PCB Boards for Encoder Signals Output

Two custom PCB boards have been designed to combine the signals from three encoders and output them to National Instruments PCI 6602 board. For every encoder, there are 10 pin outputs, shown in Figure A.7. SN75175 IC is recommended as a line receiver in Maxon catalog for better signal stability. It is a monolithic quadruple dif-

ferential line receiver with 3-state outputs. After function of line receiver, Channel $\bar{A}$ and Channel A are combined to be one channel. The same thing happens on Channel $\bar{B}$ and Channel B. The Vcc and GND from two motors are combined together.

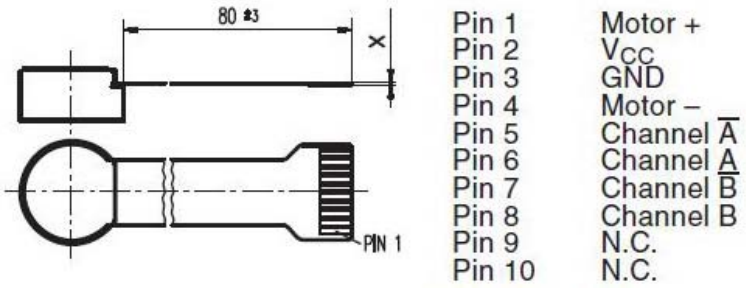

Figure A.7: Encoder Pinout

The first board is designed to combine the two motors for wrist motion. The schematics of this PCB board is shown in Figure A.8. In the figure, the bold green line is for GND. After the combination of two encoder signals and processing of SN 75175, there are only 10 pins output left, presented in Table A.6.

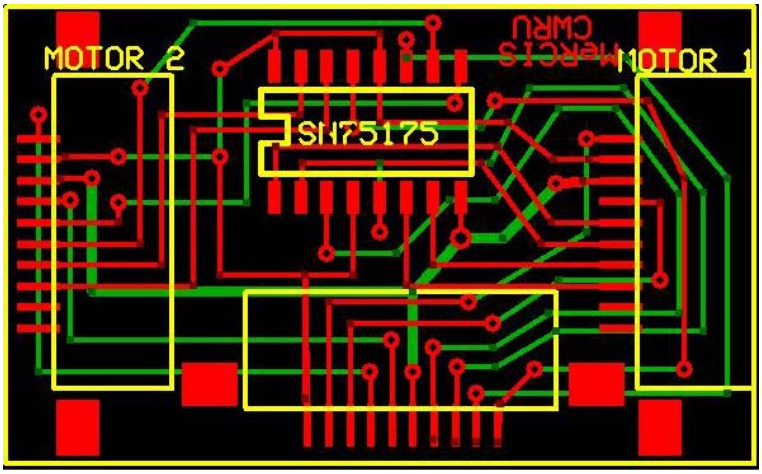

Figure A.8: PCB board for two motors

The second board is designed to combine the encoder signals from the motor for roll motion and the output of the first board. The design principle is the same as the first board. The schematic is shown in Figure A.8. There are only 16 pins output left, represented in Table A.7.

Table A.6: Pinout of PCB board for two motors

Pin Number	output
1	+Vcc
2	Motor 1+
3	Motor 1-
4	Motor 2+
5	Motor 2-
6	Gnd
7	Channel 1A
8	Channel 1B
9	Channel 2A
10	Channel 2B

Table A.7: Pinout of PCB board for one motors

Pin Number	output
1	+Vcc
2	Motor0+
3	Motor0-
4	Motor1+
5	Motor1-
6	Motor2+
7	Motor2-
8	Gnd
9	Channel 0A
10	Channel 0B
11	Channel 1A
12	Channel 1B
13	Channel 2A
14	Channel 2B
15	N.C.
16	N.C.

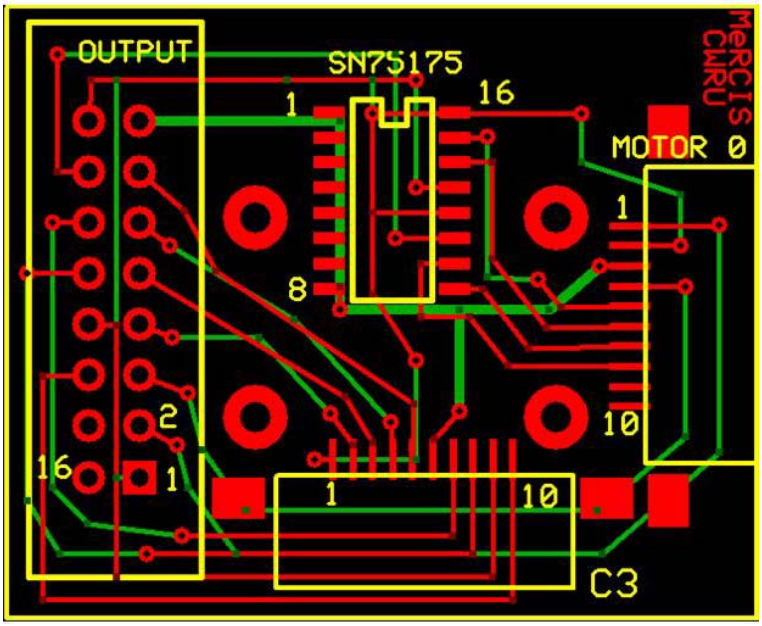

Figure A.9: PCB board for one motor

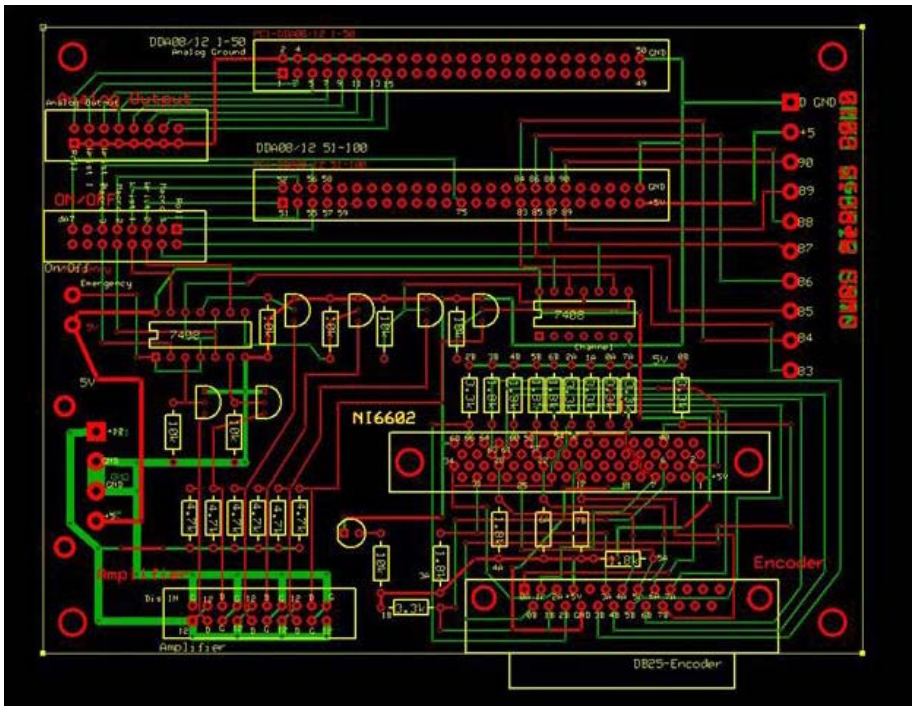

Figure A.10: Amplifier circuit board

This amplifier circuit board is designed for six motors with six encoders. Three motors are for base stage of this prototype that will be developed in future research. Other three motor are used for this prototype. The schematic of this board is shown

Table A.8: Pinout of Analog output

Signal	Pin Number	Encoder Context	Control
AO0	1	Analog Output	Motor 0
AO1	3	Analog Output	Motor 1
AO2	5	Analog Output	Motor 2
AO3	7	Analog Output	
AO4	9	Analog Output	
AO5	11	Analog Output	
AO6	13	Analog Output	
AO7	15	Analog Output	
GND	2,4,6,8,10,12,14,16	Analog Ground	GND

Table A.9: Pinout of Digital output

Signal	Pin Number	Motion Encoder	Control	16-Pin Connector	ON/OFF
DI	75	Digital Input		15	
DO0	55	Digital Output	Motor 0	1	Switch 1
DO1	53	Digital Output		3	
DO2	51	Digital Output	Motor 2	5	Switch 2
DO3	52	Digital Output	Motor 1	7	Switch 3
DO4	54	Digital Output		9	
DO5	56	Digital Output		11	

in Figure A.10. Two 50-pin connectors are mounted for DDA08/12 board. The Table A.8 represents the pinout of the analog output and the Table A.9 illustrates the pinout of digital output. A 68-pin connector for PCI-6602 board and the pinout is shown in Table A.10. A DB25 connector is used to input encoders' channel signals and the pinout is shown in Table A.11. A 20-pin connector is for amplifier power supply and the pinout is shown in Table A.12. Additionally, one 16-pin connector is intended to output analog signal as set values of amplifier. And another 16-pin located below the analog output connector is utilized to connect 'ON/OFF' swithces.

For the safety of the system, a disable circuits for amplifiers is designed, as shown in Figure A.11. According to Maxon LSC 30/2 Amplifier's operating instructions, a disable circuit with NPN transistor is recommended. If the voltage of "Dis IN" terminal on amplifier is higher than "+Vcc" -1V, the power stage becomes high impedant and the motor shaft freewheels and slows down. In the design, the disable circuit is

Table A.10: Pinout of NI 6602 board

Connector Pin	Signal	Encoder Context	DB25 Cable Pin	Counter Contex
1	+ 5V	+ 5V	4	
2	PFI 39	Channel 0A	1	
3	PFI 38			
5	PFI 36			
6	PFI 33	Channel 1B	15	
7	PFI 35	Channel 1A	2	
8	PFI 34			
9	PFI 32			
10	PFI 0			
11	D GND	D GND	17	
12	PFI 3			
13	PFI 4			
14	D GND			
15	PFI 7			
17	PFI 9	Channel 7B	22	
21	PFI 14		3	Counter 6 Gate
22	PFI 15	Channel 6A	9	
25	PFI 19	Channel 5A	8	
28	PFI 23	Channel 4A	7	
29	PFI 24			
31	PFI 27	Channel 3A	6	
32	PFI 28			
34	PFI 31	Channel 2A	3	
40	PFI 37	Channel 0B	14	
44	PFI 1			
45	PFI 2			
47	PFI 5			
48	PFI 6			
51	PFI 10		6	Counter 7 Gate
52	PFI 11	Channel 7A	10	
54	PFI 13	Channel 6B	21	
57	PFI 17	Channel 5B	20	
58	PFI 18		2	Counter 5 Gate
60	PFI 21	Channel 4B	19	
61	PFI 22		0	Counter 4 Gate
63	PFI 25	Channel 3B	18	
64	PFI 26			
66	PFI 29	Channel 2B	16	
67	PFI 30			
68	D GND			

Table A.11: Pinout of 25-pin connector

Pin Number	Signal
1	Channel 0A
2	Channel 1A
3	Channel 2A
4	+5V
5	
6	Channel 3A
7	Channel 4A
8	Channel 5A
9	Channel 6A
10	Channel 7A
11	
12	
13	
14	Channel 0B
15	Channel 1B
16	Channel 2B
17	GND
18	Channel 3B
19	Channel 4B
20	Channel 5B
21	Channel 6B
22	Channel 7B
23	
24	
25	

Table A.12: Pinout of 20-pin connector

Pin Number	Signal
1	+ 12V
2	GND
3	Dis IN
4	+ 12V
5	GND
6	Dis IN
7	+ 12V
8	GND
9	Dis IN
10	+ 12V
11	GND
12	Dis IN
13	+ 12V
14	GND
15	Dis IN
16	+ 12V
17	GND
18	Dis IN
19	+ 12V
20	GND

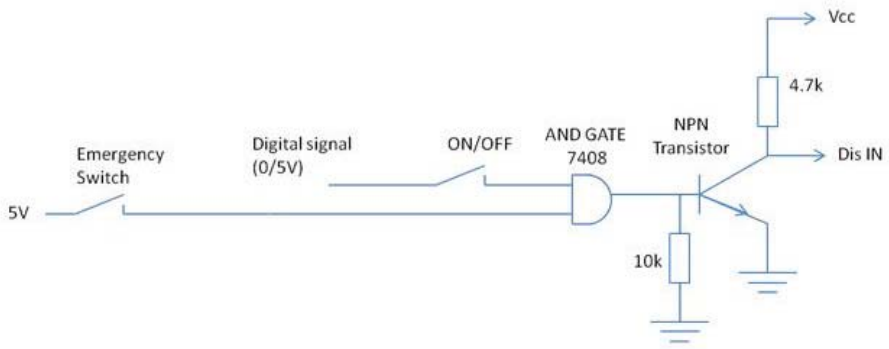

Figure A.11: Amplifier disable circuit

composed of a combination of three switches, including 'ON/OFF' mechanical switch, an emergency software switch corresponding to individual amplifier and an emergency mechanical switch relating to all amplifiers. 7408 IC And Gate outputs the result of combination of switch signals to NPN transistor. The signal from And Gate would be high level and the NPN transistor would open, enabling the amplifier, only when the 'ON/OFF' switches, the emergency mechanical switch are closed, and the digital signal is at high level. Otherwise, if any of the switches is open, the amplifier would be disable.

Bibliography

[1] M. C. Cavusoglu, W. Williams, F. Tendick, and S. S. Sastry, "Robotics for telesurgery: Second generation berkeley/ucsf laparoscopic telesurgical workstation and looking towards the future applications," *Industrial Robot, Special Issue on Medical Robotics*, vol. 30, no. 1, pp. 22–29, January 2003.

[2] *http://www.intuitivesurgical.com/index.aspx*.

[3] S. M. Gordon, "New surgical techniques and surgical site infections," *Emerg Infect Dis*, vol. 7, no. 2, pp. 217–219, March-April 2001.

[4] A. R. Lanfranco, A. E. Castellanos, J. P. Desai, and W. C. Meyers, "Robotic surgery: A current perspective," *Annals of Surgery*, vol. 239, no. 1, pp. 14–21, January 2004.

[5] U. Hagn, R. Konietschke, A. Tobergte, M. Nickl, S. Jorg, B. Kbler, G. Passig, M. Groger, F. Frohlich, U. Seibold, L. Le-Tien, A. Albu-Schaffer, A. Nothhelfer, F. Hacker, M. Grebenstein, and G. Hirzinger, "DLR mirosurge: a versatile system for research in endoscopic telesurgery," *Int J CARS*, vol. 5, no. 2, pp. 183–193, March 2010.

[6] M. O. Schurr, G. Buess, B. Neisius, and U. Voges, "Robotics and telemanipulation technologies for endoscopic surgery," *Surgical Endoscopy*, vol. 14, no. 4, pp. 375–381, April 2000.

[7] N. Simaan, K. Xu, W. Wei, A. Kapoor, P. Kazanzides, R. Taylor, and P. Flint, "Design and integration of a telerobotic system for minimally invasive surgery of the throat," *The International Journal of Robotics Research*, vol. 28, no. 9, pp. 1134–1153, September 2009.

[8] P. Berkelman and J. Ma, "A Compact, Modular, Teleoperated Robotic Minimally Invasive Surgery System," in *Proceedings of IEEE/RAS-EMBS International Conference on Biomedical Robotics and Biomechatronics, Pisa Italy*, Feburary 2006.

[9] I. V. M. Cenk Cavusoglu and F. Tendick, "Workspace Analysis of Robotic Manipulators for a Teleoperated Suturing Task," in *Proceedings of the 2001 IEEE/RSJ International Conference on Intelligent Robots and Systems, Maui, Hawaii*, October 2001.

[10] V. R. C. Kode and M. C. Cavusoglu, "Design and characterization of a novel hybrid actuator using shape memory alloy and dc micromotor for minimally invasive surgery applications," *IEEE/ASME Transactions on mechatronics*, vol. 12, no. 4, pp. 455–464, August 2007.

[11] A. M. Okamura, C. Simone, and M. D. OLeary, "Force modeling for needle insertion into soft tissue," *IEEE transactions on biomedical engineering*, vol. 51, no. 10, pp. 1707–1716, October 2004.

[12] M. P. Ottensmeyer, "Minimally invasive instrument for in vivo measurement of solid organ mechanical impedance," Ph.D Thesis, Massachusetts Institute of Technology, 2001.

[13] J. Peirs, D. Reynaerts, and H. V. Brussel, "Design of miniature parallel manipulators for integration in a self-propelling endoscope," *Elsevier*, vol. 85, pp. 409–417, August 2000.

[14] C. Reboulet and S. Durand-Leguay, "Optimal design of redundant parallel for endoscopic surgery mechanism," in *Proceedings of the 1999 IEEE/RSJ International Conference on Intelligent Robots and Systems*, 1999.

[15] J.-P. Merlet, "Micro parallel robot MIPS for medical applications," in *Proceedings of IEEE Int. Conf. on Emerging Technologies and Factory Automation, Antibes*, 2001.

[16] K. Ikuta, S. Daifu, T. Hasegawa, and H. Higashikawa, *Hyper-finger for Remote Minimally Invasive Surgery in Deep Area*, ser. Lecture Notes in Computer Science. Springer Berlin / Heidelberg, 2002, vol. 2488, pp. 173–181.

[17] N. Simaan, "Snake-Like Units Using Flexible Backbones and Actuation Redundancy for Enhanced Miniaturization," in *Proceedings of the 2005 IEEE International Conference on Robotics and Automation, Barcelona, Spain*, 2005.

[18] A. J. Madhanir, G. Niemeyer, and J. K. S. Jr., "The Black Falcon: A Teleoperated Surgical Instrument for Minimally Invasive Surgery," in *Proceedings of the 1998 IEEE/RSJ Intl. Conference on Intelligent Robots and Systems, Victoria, B.C., Canada*, 1998.

[19] U. Seibold, B. Kubler, , and G. Hirzinger, "Prototype of Instrument for Minimally Invasive Surgery with 6-Axis Force Sensing Capability," in *Proceedings of the 2005 IEEE International Conference on Robotics and Automation,Barcelona, Spain*, 2005.

[20] H. Rininsland, "Artemis. a telemanipulator for cardiac surgery," *Eur J Cardiothorac Surg*, vol. 16, pp. S106–S111, November 1999.

[21] M. Minor and R. Mukherjee, "A Dexterous Manipulator for Minimally Invasive Surgery," in *Proceedings of the 1999 IEEE International Conference on Robotics and Automation, Detroit, Michigan*, 1999.

[22] H. Yamashitaa, K. Matsumiyaa, K. Masamunea, H. Liaob, T. Chibac, and T. Dohia, "Two-dofs bending forceps manipulator of 3.5-mm diameter for intrauterine fetus surgery: Feasibility evaluation," *International Journal of Computer Assisted Radiology and Surgery*, vol. 1, pp. 218–220, June 2006.

[23] K. Yokoi, K. Komoriya, and K. Tanie, "Development of a coupled tendon drive manipulator with seven degrees-of-freedom," *Control and Information Sciences*, vol. 187, pp. 339–346, 1993.

[24] R. M. Murray, Z. Li, and S. S. Sastry, *A Mathematical Introduction to Robotic Manipulation*, 1st ed. 6000 Broken Sound Parkway NW, Suite 300, Boca Raton, FL 33487-2742: CRC Press, 1994.